Chapter 4
Computer Simulation of Side-Chain Liquid Crystal Polymer Melts and Elastomers

Jaroslav M. Ilnytskyi, Marina Saphiannikova, Dieter Neher, and Michael P. Allen

The combination of liquid-crystalline (LC) groups and a polymeric matrix is particularly appealing to the materials scientist, in view of the large number of applications which exist for both parent subsystems (Chung 2008). Moreover, composite systems of this type, LC polymers, exhibit a synergy, i.e. the presence of properties not observed in their constituent parts.

This is particularly true for side-chain liquid crystal polymers (SCLCPs) containing photo-active chromophore groups. Such photoactive SCLCPs find their application in modern photonics, electronics and opto-mechanics. In particular, these are successfully used to produce alignment layers for LC fluorescent polymers in display and semiconductor technology (Sainova et al. 2002; Zen et al. 2002), to build waveguides and waveguide couplers (Viswanathan et al. 1999; Natansohn and Rochon 1999), as data storage media (Berg et al. 1996; Rasmussen et al. 1999; Zilker et al. 1998; Stracke et al. 2000), as labels in quality product protection (Stiller et al. 2005), and in a number of other applications.

J.M. Ilnytskyi (✉)
Institute for Condensed Matter Physics of National Academy of Sciences of Ukraine,
1, Svientsitskii Str., 79011 Lviv, Ukraine
e-mail: iln@icmp.lviv.ua

M. Saphiannikova
Leibniz-Institut für Polymerforschung Dresden e.V., Hohe Strasse 6, 01069 Dresden, Germany
e-mail: grenzer@ipfdd.de

D. Neher
Institute for Physics and Astronomy, University of Potsdam, Karl-Liebknecht-Strasse 24-25, 14476 Potsdam-Golm, Germany
e-mail: neher@uni-potsdam.de

M.P. Allen
Department of Physics, University of Warwick, Coventry CV4 7AL, UK

H.H. Wills Physics Laboratory, Royal Fort, Tyndall Avenue, Bristol BS8 1TL, UK
e-mail: m.p.allen@warwick.ac.uk; m.p.allen@bristol.ac.uk
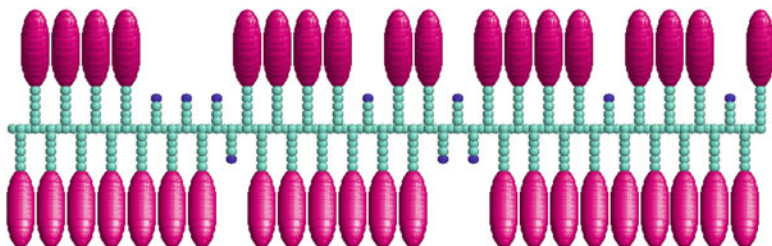
Fig. 4.1 Schematic representation of a single SCLCP molecule. *Green-gray spheres*: hydrocarbon groups. *Magenta ellipsoids*: mesogen groups (including the case of chromophores). *Blue spheres*: chemically reactive groups intended to crosslink into a polymer network (elastomer). Reproduced from Ilnytskyi et al. (2012) with permission from The Royal Society of Chemistry

Schematically, a single SCLCP molecule is shown in Fig. 4.1. It contains a backbone and pendant spacer chains, some of which are terminated by a mesogen (including the case of chromophore mesogens). The length of the backbone is L_b monomers, whereas that of each spacer is L_c. The branching functionalization of the SCLCP is constant and equal to k_f; therefore, the number of attached side-chains is equal to $N_c = L_b/k_f$. The bulk phase behavior of such systems free of mechanical or optical perturbations is well studied experimentally (Collings and Hird 2001; Rutloh et al. 2000; Freiberg et al. 2003). An important factor in their phase diagram is the amount of coupling between the chromophores and the backbone, which is determined by the spacer length, L_c. For large values of L_c, both subsystems are decoupled, and microphase separation drives the system into lamellar smectic phase(s). For instance, one or several smectic phases are observed for the siloxane SCLCP at $L_c \geq 6$. With the decrease of L_c the coupling between the two subsystems increases and either nematic ($L_c = 3 - 5$) or even no LC phases ($L_c \leq 2$) are found (Collings and Hird 2001). In the latter case, the SCLCP is characterized by a high glass transition temperature, T_g, and is in an amorphous state at room temperature. Other factors defining the phase diagram of real SCLCPs are the transient dipole moment of LC groups, steric effects, etc. (Collings and Hird 2001).

External stimuli applied to the SCLCP melt, in the form of mechanical deformation, illumination (for photo-sensitive SCLCPs), or by other means, generate internal stress in the material. Due to the viscoelasticity of the material, it is relaxed via deformation (at short time scales) and via flow (at large time scales), unless the diffusion of the system is suppressed by jamming it in between substrate plates. The exact scenario for the stress relaxation is highly dependent on details of the molecular architecture.

Another way to suppress the diffusivity of the system on large time scales is to perform crosslinking of the melt. As a result, side-chain liquid crystal elastomers (SCLCEs) can be formed, the systems fabricated experimentally since the 1980s (Finkelmann et al. 1981, 1984). Their mechanical properties are similar to the case of non-LC polymer networks in terms of high elasticity, whereas the response to external electromagnetic stimuli is driven by the LC groups. Due to coupling

between these two constituent subsystems, a number of opto- and thermo-mechanical effects are observed in SCLCEs, bringing them into the wider class of shape-memory polymers (Behl and Lendlein 2007; Ahn et al. 2011). For instance, reversible shape changes at the LC order-disorder transition provide a basis for applications of SCLCE as low-frequency actuators and sensors (i.e. artificial muscles) (Shenoy et al. 2002; Spillmann et al. 2007). A separate class of technologically interesting materials are SCLCEs containing chromophore groups (Ikeda et al. 2007).

4.1 Side-Chain Liquid Crystal Polymers: Modelling of Equilibrium Properties

4.1.1 Semi-atomistic Molecular Dynamics Modelling

Practically reasonable system sizes for atomic-resolution simulations of LC melts and networks lie within the 10–100 nm range, well below the typical dimensions of real physical samples that demonstrate elasticity. In this context, the issue arises of how phenomena occurring at smaller length scales in such a material influence its macroscopic behavior. As discussed in Hill (1984, 1985) and Matouš and Geubelle (2005), at the micro-level the material response is heterogeneous, whereas at the macro-level it appears homogeneous. One could explain this by averaging the material properties over a large number of inhomogeneous fragments [in the same way that "self-averaging" applies to the description of disordered critical systems (Aharony and Harris 1996; Binder 1986; Wiseman and Domany 1998)]. Therefore, when performing mapping of the properties of a small system onto those of a larger one, several issues should be considered. First of all, for the case of SCLCEs, we assume the affine deformation of a small volume element. Secondly, a reduction of both the number and the length-scale of the structural inhomogeneities is performed. For instance, better homogeneity of the polymer network can be achieved by performing spatially-controlled crosslinking. One can also imitate self-averaging within a larger system by averaging the properties of interest obtained for a number of different replicas of the small-size system. All this brings the properties obtained for the small-size system closer to those for their larger counterpart. More discussion of computational approaches addressing the relation between micro- and macro-scales in composite systems can be found elsewhere (Matouš and Geubelle 2005; Michel et al. 1999).

   The model used in this study belongs to the class of semi-atomistic models, in which a group of atoms is treated as a single particle. It is a classical mechanical description, which focuses on the most relevant features of the LC polymers, namely the (variable) flexibility of polymer chains and the ability of mesogens to form LC phases. For the case of the SCLCP molecule shown in Fig. 4.1, two types of particle would suffice. These are spherically-symmetrical particles representing

hydrocarbon CH_n groups, and anisometric ones representing elongated mesogens. Such models have proven to be successful in a number of studies (Stimson and Wilson 2005; Wilson 1997; McBride and Wilson 1999; Wilson et al. 2003, 2005). The set of potentials that govern interaction within the polymer scaffold are united-atom force fields, developed for branched alkanes by various groups, e.g. by Vlugt et al. (1999). These are normally split into bonded and non-bonded interactions. The bonded interactions include bond stretching V_b, bond angle bending V_a, pseudo bond angle bending V_z (see below) and torsional V_t energy terms given by the following expressions

$$V_b = \sum_{i=1}^{N_b} \frac{k_b}{2} (\ell_i - \ell_0)^2, \tag{4.1a}$$

$$V_a = \sum_{i=1}^{N_a} \frac{k_a}{2} (\vartheta_i - \vartheta_0)^2, \tag{4.1b}$$

$$V_z = \sum_{i=1}^{N_z} \frac{k_z}{2} (\zeta_i - \zeta_0)^2, \tag{4.1c}$$

$$V_t = \sum_{i=1}^{N_t} \sum_{n=1}^{3} C_n \cos{}^n \phi_i, \tag{4.1d}$$

where ℓ_i, ϑ_i, ζ_i and ϕ_i denote the i-th bond length, bond angle, pseudo bond angle and torsion angle, respectively. Their respective totals are N_b, N_a, N_z and N_t. We consider different parameters for the hydrocarbon groups: CH, CH_2 and CH_3. Then, ℓ_0, ϑ_0 and ζ_0 are the reference bond length, valence angle and pseudo bond angle, respectively. The energy term V_z was introduced by Wilson (1997), where ζ_i is measured between the long axis of the i-th mesogen and the direction of the bond that connects it to the last pseudo-atom of a spacer (here the value for the reference angle $\zeta_0 = \pi$ is used). This interaction prevents the mesogen from unphysical free rotations with respect to the last atom of the spacer. The torsional energy V_t has a Ryckaert–Bellemans form (Ryckaert and Bellemans 1975) with the chain stiffness defined via the set of constants, C_n. In our simulations we consider two cases: flexible chains and stiff chains with different sets of constants C_n. The force-field constants used in this study are given below.

The non-bonded interactions include the hydrocarbon–hydrocarbon, mesogen–mesogen and mixed hydrocarbon–mesogen terms. The hydrocarbon–hydrocarbon interaction is of the Lennard-Jones form:

$$V_{aa} = \sum_{\langle ij \rangle} \left[\frac{a_i a_j}{r_{ij}^{12}} - \frac{c_i c_j}{r_{ij}^6} \right], \tag{4.2}$$

where r_{ij} is the distance between the i-th and the j-th particles, and a_i, c_i are factorized Lennard-Jones energy parameters. The mesogens are considered to be

rigid anisometric objects that interact via the Gay–Berne potential (Gay and Berne [1981]):

$$V_{mm} = \sum_{\langle i j \rangle} 4\varepsilon_{ij}\left[(\rho_{ij})^{-12} - (\rho_{ij})^{-6}\right], \tag{4.3}$$

where ε_{ij} and ρ_{ij} are effective energy and reduced distance parameters, respectively, and both are functions of the mesogen orientations $\mathbf{e}_i$, $\mathbf{e}_j$ and their interconnecting vector $\mathbf{r}_{ij}$. Complete expressions can be found elsewhere (Gay and Berne [1981]). Similar expressions can be derived for the mixed interactions between the i-th hydrocarbon and j-th mesogen, using the extended Gay–Berne potential (Cleaver et al. [1996]):

$$V_{am} = \sum_{\langle i j \rangle} 4\varepsilon'_{ij}\left[(\rho'_{ij})^{-12} - (\rho'_{ij})^{-6}\right]. \tag{4.4}$$

The meaning of ε'_{ij} and ρ'_{ij} is similar to that for ε_{ij} and ρ_{ij}; more details can be found elsewhere (Wilson [1997]; Ilnytskyi and Wilson [2001]). The Lennard-Jones interactions are cut at $r_c = 9.8$Å and the long-range correction to the potential energy and the virial are evaluated (Allen and Tildesley [1989]), while the Gay–Berne and mixed interactions are cut at $r_c = 18.9$ Å and $r_c = 16.5$ Å, respectively, and shifted in such a way that $V_{mm} = 0$ and $V_{am} = 0$ when $r = r_c$.

Here we will list a complete set of force-field parameters used in the simulations. Masses are 0.232×10^{-25}kg for the spherical particles and 0.375×10^{-24}kg for the mesogens; the moment of inertia for the latter is 0.469×10^{-23}kg Å^2. The pairs of $\{a, c\}$ energy parameters for the Lennard-Jones potential V_{aa} are: $\{2112.19, 39.4193\}$, $\{1877.05, 30.9202\}$ and $\{1222.83, 17.7425\}$ for CH_3, CH_2 and CH particles, respectively, all in units of $(10^{-20}J)^{1/2}$ and length units of Å. The parameters of the Gay-Berne potential are as follows: $\sigma_0 = 5$Å, $\varepsilon_0 = 0.561 \times 10^{-20}$ J, $\kappa = 3$, $\kappa' = 5$, $\mu = 1$, $\nu = 2$, where we follow the designations of Gay and Berne ([1981]). The bond length ℓ_0 in the expression for V_b is 1.540Å and 7.075Å for sphere-sphere and sphere-mesogen bonds, respectively; the bond energy constant is $k_b = 361.291 \times 10^{-20}$ J/Å^2 in both cases. The bond angle ϑ_0 in the expression for V_a is 1.9897rad and 1.9548rad for linear and branched chain fragments, respectively; the bend energy constant is $k_a = 86.291 \times 10^{-20}$ J/rad^2 in both cases. The parameters of the pseudo bond angle interaction V_z are chosen as $\zeta_0 = \pi$ and $k_z = k_a$. Finally, the set of constants C_n for the torsional potential V_t are used to tune the flexibility of chains. For the case of flexible chains we use the following sets (all in units of 10^{-20} J): $\{1.3941, 2.7868, 0.18824, -4.3691\}$ and $\{0.51505, 1.2689, 0.37022, -2.3984\}$ for linear and branched fragments, respectively. For stiff chains the following set is used: $\{1.79, 5.57, 1.38, -8.74\}$ in the same energy units.

The MD simulations are performed with the aid of the parallel program GBMOLDD (Ilnytskyi and Wilson [2001], [2002]). A simulation box of dimensions L_x, L_y and L_z, with periodic boundary conditions, that mimicks the behavior of a volume element

in the bulk, is used. We employed the $NP_{xx}P_{yy}P_{zz}T$ ensemble, that is a simplified version of the Parrinello-Rahman scheme (Parrinello and Rahman 1981), where only the principal stresses, $\sigma_{xx}, \sigma_{yy}, \sigma_{zz}$ are constrained (the equations of motion can be found in Ilnytskyi and Neher (2007)). Two types of simulation are undertaken in this study: under atmospheric pressure, P_{atm}, and under external uniaxial load. In the first case, all three principal stresses are constrained at the same value of P_{atm}. In the second case, a load P_L is introduced along one of the axes, $\alpha = \{x, y, z\}$, by constraining $\sigma_{\alpha\alpha}$ to $P_{atm} - P_L$, whereas both other stresses, $\sigma_{\beta\beta}$ and $\sigma_{\gamma\gamma}$ are constrained at $P_{atm} + P_L/2$. In this way the trace of the stress tensor is always equal to $3P_{atm}$. For the integration of the equations of motion we used the leap-frog algorithm; the RATTLE constraint has been applied for the integration of the mesogen rotation (Ilnytskyi and Wilson 2002). A time step $\Delta t = 2\,\text{fs}$ was found to be acceptable for all production runs.

The anisotropic deformation of the simulation box at each time instant t is monitored via the three principal strains, $\varepsilon_\alpha = L_\alpha(t)/L_\alpha(0)$, where $L_\alpha(t)$ is the dimension of the box along the corresponding spatial axis α at time t. We define the strain along the symmetry axis (e.g. nematic director, axis of applied load, etc.), as $\varepsilon_\parallel = L_\parallel(t)/L_\parallel(0)$.

To characterize the LC order of the mesogens, we evaluate the nematic order parameter with respect to the director, S_2, and also the order parameters S_α evaluated with respect to each spatial axis α:

$$S_2 = \langle P_2(\cos\theta_i)\rangle_i, \quad S_\alpha = \langle P_2(e_{\alpha,i})\rangle_i. \tag{4.5}$$

Here, $P_2(x) = \frac{1}{2}(3x^2 - 1)$ is the second Legendre polynomial, and θ_i is the angle between i-th mesogen orientation $\mathbf{e}_i$ and the nematic director. The components of $\mathbf{e}_i$ are denoted $e_{\alpha,i}$ and the averaging is performed over all the mesogens within the system.

The distribution of the particles of the k-th polymer chain in space is characterized by the components of the gyration tensor:

$$G_{\alpha\beta}^{[k]} = \frac{1}{N}\sum_{i=1}^{N}(r_{i,\alpha}^{[k]} - R_\alpha^{[k]})(r_{i,\beta}^{[k]} - R_\beta^{[k]}). \tag{4.6}$$

Here i indexes the particle with position $r_{i,\alpha}^{[k]}$ which belongs to k-th chain, and $\mathbf{R}^{[k]}$ is the position of the center of mass of the k-th chain. The gyration tensor can be rotated into a particular frame (e.g. one related to the nematic director). Let us denote the components of the rotated tensor as $Q_{\alpha\beta}^{[k]}$ and their averages over similar chains and over time as $Q_{\alpha\beta} = \langle Q_{\alpha\beta}^{[k]}\rangle_{k,t}$. These components provide an average distribution of particles with respect to the axes of the required frame. Other properties are also used, namely the average radius of gyration R_g, defined via:

$$R_g^2 = \sum_{\alpha=1}^{3} Q_{\alpha\alpha}, \tag{4.7}$$

as well as the anisotropy of the gyration tensor with respect to a prescribed axis α (e.g. the director, axis of applied load, etc.):

$$\frac{R_{\parallel}}{R_{\perp}} = \frac{\sqrt{Q_{\alpha\alpha}}}{\left(\sqrt{Q_{\beta\beta}} + \sqrt{Q_{\gamma\gamma}}\right)/2}, \tag{4.8}$$

where β, γ stand for the other two axes perpendicular to α. The shape anisotropy of backbones and side-chains is also characterized by the relations between the average semi-axes of their equivalent ellipsoids. In this case the components of $G_{\alpha\beta}^{[k]}$ are not averaged, but the tensor is diagonalized for each chain k and the squared semiaxes $(\sigma_{\alpha}^{[k]})^2$ are found as its eigenvalues. These are then averaged over k and over time to yield the average values $\sigma_{\alpha}^2 = \langle(\sigma_{\alpha}^{[k]})^2\rangle_{k,t}, \qquad \sigma_1^2 > \sigma_2^2 > \sigma_3^2$. Finally, the average end-to-end distance R_{1N} for particular types of chain (backbones, side-chains, etc.) can also be evaluated from its square as

$$R_{1N}^2 = \left\langle \sum_{\alpha=1}^{3} [r_{1,\alpha}^{[k]} - r_{N,\alpha}^{[k]}]^2 \right\rangle_{k,t}. \tag{4.9}$$

4.1.2   Properties of SCLCP in a Weak Coupling Limit

We will study the phase behavior of the SCLCP model shown schematically in Fig. 4.1 in two limiting cases. Let us proceed to the first one, the "weakly-coupled" model, which describes the SCLCP where the two subsystems, backbone and mesogens, are essentially decoupled. The backbone is assumed to be flexible (mimicking a methacrylate or similar chain), while the spacer length is relatively long. The parameters chosen for our analysis are: $L_b = 39$, $L_c = 10$, functionalization $k_f = 4$, the number of attached side-chains $N_c = 10$.

The initial configuration was built of 64 SCLCP molecules with a regular double-layered lamellar arrangement. The melting runs were undertaken for up to 16 ns. The simulations were performed in the $NP_{xx}P_{yy}P_{zz}T$ ensemble at atmospheric pressure, and at a set of temperatures ranging from 450 to 600 K. The melt of SCLCPs preserves a stable smectic order at $T = 485$K and below, and melts quickly into the isotropic phase when annealed to $T > 520$K. At intermediate temperatures, $T = 490\text{-}495$ K, the smectic phase melts slowly. Therefore, we estimated the smectic to isotropic (SI) transition temperature to be $T_{SI} \sim 490$K. No evidence for the nematic phase was found, in agreement with the phase diagrams of real SCLCPs with a long (6–10 hydrocarbons) spacer and syndiotactic structure (Collings and Hird 2001).

After these preliminary estimates for the order–disorder transition temperature, a smectic phase was grown out of the isotropic phase. Due to the small system size and the possibility for the system to be locked in a metastable state (typical for the molecular dynamics simulation of viscous systems), the growth of the smectic

phase was assisted by applying an external uniaxial field. This affects the orientations of the mesogens and is introduced via the rotational energy

$$U_i^{\text{Field}} = -F \cdot P_2(\cos \theta_i), \qquad (4.10)$$

where $F > 0$ is the field strength, θ_i is the angle between the long axis of the i-th mesogen and the direction of the field. Throughout this study we will use the reduced field strength, f, where $\text{F} = f \cdot 10^{-20}$ J. The field-assisted growth of the smectic phase was performed close to the transition, at $T = 490$K.

The value of the field strength f determines the reorientation rate of the mesogens and it has a profound effect on the formation of the smectic phase. If the mesogen reorientation rate is of the same order as the equilibrium relaxation times for backbones and side-chains, then concerted rearrangement of the molecules as a whole takes place. This is indicated in Fig. 4.2, where the evolution of the orientational order parameters S_2 is shown at $f = 0.2$ for the mesogens and for the long axes of equivalent ellipsoids for backbones and side chains (solid symbols). After the field is switched off and the temperature is reduced to 485 K, the smectic order remains stable in all subsystems (see open symbols). Therefore, one may conclude that the system is steered successfully into a global minimum state. However, when a stronger field is applied, $f > 0.5$, the reorientation rate of the mesogens does not conform with those for the polymer chains. As a result, when the field is switched off and the temperature is reduced, the system evolves into a metastable polydomain, globally isotropic state (Ilnytskyi and Neher 2007).

The smectic phase, a snapshot of which is depicted in Fig. 4.3, has a structure typical of a microphase-separated lamellar phase. It is of a "sandwich" type made of alternating layers of mesogens, side-chains and backbones. The real LCSCP system microphase separates due to poor miscibility between alkyl chains and mesogens containing aromatic groups. In our model, this effect is mapped onto poor miscibility between spherical and elongated particles. However, the shape characteristics of the polymer chains display only minor changes when undergoing the isotropic–smectic
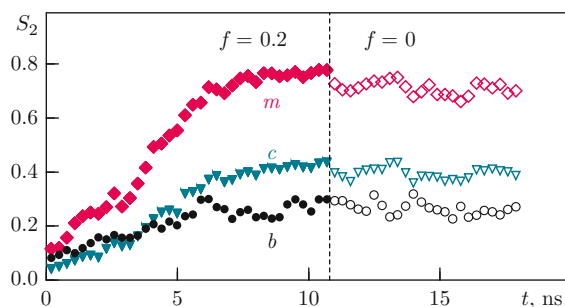
Fig. 4.2 Evolution of the orientational order parameters for the mesogens (m), side chains (c) and backbones (b) during the field-induced growth of the smectic phase: $f = 0.2$, $T = 490$ K (*filled symbols*) and during the relaxation with no field: $f = 0.0$, $T = 485$ K (*open symbols*). Reprinted with permission from Ilnytskyi and Neher (2007). Copyright 2007, AIP Publishing LLC
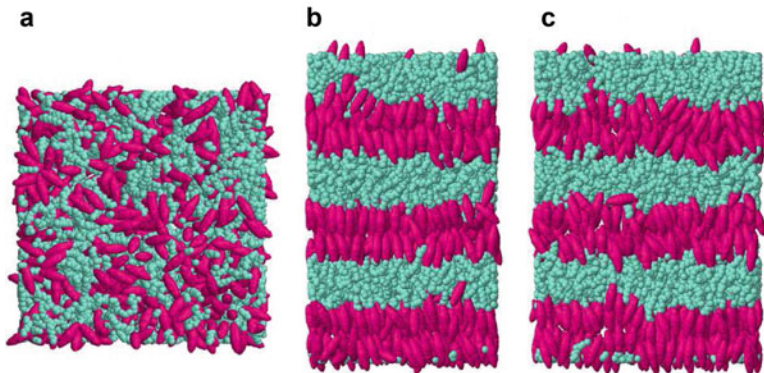
Fig. 4.3 Snapshots showing different stages of the monodomain smectic phase growth. (**a**) Initial isotropic state at $T = 490$K; (**b**) smectic structure formed at $T = 490$K with the aid of the field $f = 0.2$; (**c**) the same structure relaxed at $T = 485$K with the field switched off. (**a**), (**b**), (**c**) represent system states at $t = 0$, $t = 11$ns and $t = 18$ns, as shown in Fig. 4.2

Table 4.1 Average shape parameters for the backbones and side-chains in the isotropic and smectic phases, see text for the notations; $R_{1N}{}^4$ is defined as the fourth moment of the end-to-end distance, analogous to Eq. (4.9) for $R_{1N}{}^2$.

Chains	Backbones		Side-chains		
Phase	Isotropic	Smectic	Isotropic	Smectic	Gaussian
R_g^2, Å^2	62(4)	66(3)	10.4(1)	10.9(1)	
R_{1N}^2, Å^2	410(30)	460(30)	86(2)	94(1)	
R_{1N}^2/R_g^2	6.7(3)	6.9(3)	8.27(7)	8.58(4)	6
$R_{1N}^4/(R_{1N}^2)^2$	1.4(1)	1.5(1)	1.06(1)	1.04(1)	5/3
σ_2^2/σ_3^2	3.5(3)	3.7(3)	4.3(1)	4.1(1)	2.5
σ_1^2/σ_3^2	18(2)	20(2)	48(2)	57(2)	11.8

Numbers in parentheses are estimated errors in the last quoted digit. Exact values (where appropriate) for the Gaussian chain are also provided

transition. These are shown in Table 4.1 for the backbones and side-chains. As one can see from the relevant columns, backbones demonstrate no changes in their shape, whereas the side-chains become more anisotropic in the smectic phase, as evidenced by the increase of the σ_1^2/σ_3^2 ratio by 19 %. Backbones and, to a much greater extent, the side chains, adopt conformations that deviate from that of the ideal Gaussian chain. This effect can be explained by specific topological constraints in the SCLCP structure. Specifically, the side chains are grafted to the backbone at one end and have a large mesogen unit attached at another end. Clearly, this restricts their conformational freedom.

Given the minor influence of the phases on the shape properties of the backbones and side-chains, the difference, as also evidenced in Fig. 4.3, should be reflected in their spatial arrangement. The averaged mass distribution of chains in space is given by the components of the gyration tensor rotated into the director frame, $Q_{\alpha\alpha}$, introduced above. The values for $Q_{\alpha\alpha}$ in the isotropic and smectic phases are

Table 4.2 Averaged diagonal components of the mass distribution tensor in the director frame for backbones and side-chains in the isotropic and smectic phases

Chains	Backbones		Side-chains	
Phase	Isotropic	Smectic	Isotropic	Smectic
Q_{xx}	20(2)	28(2)	3.5(2)	2.3(1)
Q_{yy}	21(2)	31(3)	3.4(1)	2.3(1)
Q_{zz}	21(2)	7(1)	3.5(1)	6.2(1)

Numbers in parentheses are estimated errors in the last quoted digit

compared in Table 4.2 for both the backbones and the side-chains. As one can see, the mass distribution of the backbones and side chains in the smectic phases is markedly different from that in the isotropic phase. For the side-chains, $Q_{zz} > \frac{1}{2}(Q_{xx} + Q_{yy})$ in the smectic phase, indicating that the mass distribution of these follows the orientation of the mesogens. In this way the fragment of a mesogen plus a side-chain behaves similarly to low-molecular-weight LC molecules like the n-CB cyanobiphenyls. For the backbones, $Q_{zz} < \frac{1}{2}(Q_{xx} + Q_{yy})$ in the same phase, corresponding to their confinement in the relatively thin layers perpendicular to the nematic director. This quantifies the visual appearance of the smectic phase, provided in Fig. 4.3. Such a microphase-separated lamellar structure of the smectic phase mimics that of the experimental systems (Dimitrova 2000; Stimson and Wilson 2005).

The lamellar structure of the smectic phase manifests itself also through an essential anisotropy of the internal dynamics of its constituent fragments. This dynamics can be monitored by following the behavior of the mean-square displacement of each fragment k (e.g. backbone), defined as

$$g(t) = \left\langle \left[\mathbf{R}^{[k]}(t) - \mathbf{R}^{[k]}(0) \right]^2 \right\rangle, \tag{4.11}$$

where $\mathbf{R}^{[k]}(t) = \{X^{[k]}(t), Y^{[k]}(t), Z^{[k]}(t)\}$ is the center-of-mass position (COM) of the k-th fragment at time t. In the smectic phase we are interested in the parallel and perpendicular contributions (relative to the mesogen director):

$$g^{\perp}(t) = \left\langle \left[X^{[k]}(t) - X^{[k]}(0) \right]^2 + \left[Y^{[k]}(t) - Y^{[k]}(0) \right]^2 \right\rangle, \tag{4.12a}$$

$$g^{\parallel}(t) = \left\langle \left[Z^{[k]}(t) - Z^{[k]}(0) \right]^2 \right\rangle. \tag{4.12b}$$

On a long time scale the macromolecules behave diffusively (Doi and Edwards 1994):

$$\lim_{t \to \infty} g(t) = 6Dt, \qquad \lim_{t \to \infty} g^{\perp}(t) = 4D^{\perp}t, \qquad \lim_{t \to \infty} g^{\parallel}(t) = 2D^{\parallel}t, \tag{4.13}$$

where $D, D^{\perp}$ and $D^{\parallel}$ are the corresponding diffusion coefficients. It is obvious that if the macromolecule reaches the diffusive regime, then this will also hold for its

Table 4.3 Diffusion coefficients D_m, D_b, D_c for the mesogen, backbone and side chain centers-of-mass, respectively, in isotropic and smectic phases. The parallel and perpendicular contributions are presented in the latter case

Phase	Isotropic				Smectic	
T	600 K	520 K	495 K	485 K	485 K	
					$D^\perp$	$D^\parallel$
D_m	194(6)	159(7)	48(2)	36(2)	40(8)	5.76(6)
D_b	195(8)	157(8)	46(4)	26(3)	38(0)	0.06(3)
D_c	194(7)	158(7)	47(4)	30(2)	40(8)	0.95(7)

constituents. We estimated the diffusion coefficient D separately for the backbones, side-chains and mesogens. Runs of about 10 ns in duration were used, with mean-square displacements computed up to two-thirds of this time with reasonable statistics. Diffusion coefficients were estimated from linear fits to $g(t)$ at long times, according to Eq. (4.13). The results are collected in Table 4.3. In the smectic phase the diffusion is found to be severely hampered along the mesogen director. $D^\parallel$ is one to three orders of magnitude smaller than $D^\perp$ (see last two columns of Table 4.3). $D^\perp$ is found to be almost the same as in the overcooled isotropic phase, prepared by cooling the isotropic phase at $T = 495$K down to $T = 485$K with no aligning field. This means that all the constituents of the polymer subsystem are still very mobile in the planes perpendicular to the nematic director. These properties of the isotropic and smectic phases are relevant to our studies of the behavior of SCLCPs and SCLCEs under external perturbations, considered in the subsequent sections.

4.1.3 Properties of SCLCP in a Strong Coupling Limit

The strongly-coupled model is characterised by the following parameters: $L_b = 39$, $L_c = 2$, functionalization $k_f = 4$, the number of attached side-chains $N_c = 10$. Both backbone and spacers are modelled as stiff chains with appropriate parameters $\{C_i\}$ for the torsional potential V_t, discussed in detail at the beginning of Sect. 4.1. In our simulations, 96 side-chain molecules are packed into the simulation box in a regular geometric way (5664 polymer beads and 960 azobenzenes in total). This configuration is first heated up to $T = 700$K to erase the memory of the initial packing. After that the melt was cooled down to $T = 500$K and equilibrated for 10 ns. To be able to relate the simulation temperatures to that of the glass transition, T_g, we performed a rather brief simulation. This was done via step-by-step cooling of the melt within the temperature interval $T \in [350\text{K}, 500\text{K}]$. The temperature was reduced in steps of 10–25 K by resetting it to a lower value and then allowing the system 4–8 ns to equilibrate. The glass transition temperature T_g is then estimated from the change of the slope in the density–temperature plot, see Fig. 4.4, and found to lie between 440 and 450K.

Fig. 4.4 Estimate of the
glass transition temperature
$T_g \sim 445K$ from the change
of slope in a density–
temperature plot, in the
strongly coupled model.
Reprinted with permission
from Ilnytskyi et al. (2011).
Copyright 2011, AIP
Publishing LLC
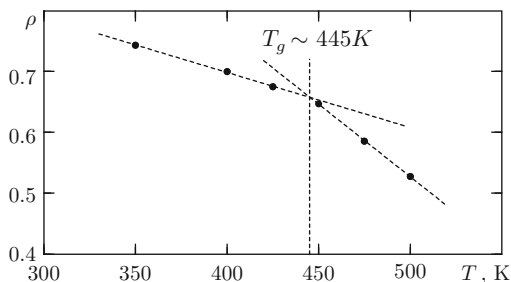
We should remark here that a thorough study of the system behavior at and
below T_g, as well as a more precise estimate for T_g itself depending on cooling rate,
is beyond the scope of this chapter. Otherwise, extremely long special purpose
simulations, and application of special techniques, would be required (Han
et al. 1994; Lyulin et al. 2003). Besides that, the glass transition in a polymer LC
can be associated not only with a freezing of the torsion angles (as in an ordinary
polymer) but also with a strengthening of the LC interaction.

To look for the possibility for forming a monodomain nematic or smectic phase,
we applied an external uniaxial aligning field, similarly to the case of the weakly-
coupled model, Eq. (4.10). These attempts were unsuccessful and no stable
monodomain ordered phases were found, in accordance with the typical phase
diagrams of side-chain LC polymers with short spacers (Collings and
Hird 2001; Rutloh et al. 2000; Freiberg et al. 2003). Instead, the polymer was
found to adopt a polydomain LC phase, with strong intradomain LC interactions,
which act as physical crosslinks (Gallani et al. 1994).

4.2 Photo-Induced Deformations in SCLCP

The isomerization state of photo-active mesogens (chromophores) can be manipu-
lated by suitable illumination. The most well-known example is azobenzene, which
undergoes a photoisomerization from the prolate *trans* to bent *cis* isomer and *vice
versa*, see Fig. 4.5. In the case of an azobenzene-containing SCLCP, the
photoisomerization induces changes in the LC subsystem and, via coupling to the
polymer component, generates internal stress in the material. The exact micro-
scopic mechanism of the stress relaxation depends on the details of the polymer
molecular architecture. This was clearly demonstrated in the experimental work of
Bublitz et al. (2000) via illumination of free-floating azo-polymer droplets with a
uniform linearly polarized beam. In the case of the polymer P6a12 (a molecular
architecture with weak coupling) the droplet was found to contract along the
polarization vector. On the contrary, in the case of the polymer E1aP
(a molecular architecture with stiff backbone and strong coupling) the droplet
was found to extend along the polarization vector (Bublitz et al. 2000). These

Fig. 4.5 The photoisomerization of azobenzene chromophores. Reprinted with permission from Ilnytskyi et al. (2011). Copyright 2011, AIP Publishing LLC
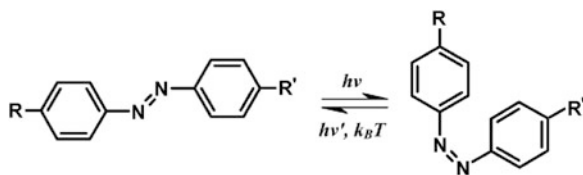
findings are closely related to the bending of azobenzene-containing elastomers when illuminated (Camacho-Lopez et al. 2004; Ikeda et al. 2007). In yet another experiment, a linearly polarized beam was applied through an optical mask with light stripes. In this case, either hills or trenches were observed in illuminated areas, again depending on the details of the polymer (Holme et al. 1999). Under spatially modulated illumination (a holographic-like setup) the even more striking effect of surface relief grating (SRG) formation was discovered in 1995 (Rochon et al. 1995; Kim et al. 1995), which has received considerable attention since then (Viswanathan et al. 1999; Oliveira et al. 2002; Hvilsted and Ramanujam 2001; Barrett et al. 2007).

SRGs can be inscribed in both weakly- and strongly-coupled azo-polymers (for reviews, see Viswanathan et al. 1999; Oliveira et al. 2002; Barrett et al. 2007). The effect is puzzling in the way that SRG formation takes place in amorphous azo-polymers well below the glass transition temperature T_g. Several models (Barrett et al. 1998; Kumar et al. 1998; Lefin et al. 1998; Pedersen et al. 1998; Baldus and Zilker 2001; Bublitz et al. 2001; Gaididei et al. 2002; Oliveira et al. 2002) have been suggested towards the explanation of the origin of the inscribing force, but none of them describes satisfactorily the light-induced motion of the azobenzene polymers at a molecular level (Saphiannikova et al. 2004; Saphiannikova and Neher 2005). Some of them assume a considerable degree of photoinduced plasticization, at least comparable with that at the glass transition. However, only very weak plasticization has been found in mechanical experiments (Mechau et al. 2002, 2005), leading to the conclusion that illumination of an azobenzene polymer layer with actinic light cannot induce a transition into a macroscopic low-viscosity melt. A thermodynamic theory, valid for amorphous azo-polymers with weak interactions between azobenzenes, was developed in Saphiannikova and Neher (2005) and Toshchevikov et al. (2009). A number of optical setups can be used to produce the SRG, in particular, ones utilizing linearly and circularly polarized light [for more details, see review papers (Viswanathan et al. 1999; Oliveira et al. 2002)]. Nunzi and coworkers demonstrated that the use of an incoherent light source is also efficient for the deformation of azopolymer nanospheres (Barillé et al. 2010), and for printing a well organized pattern at the surface of an azopolymer thin film (Kandjani et al. 2005). In our study we focus our attention on the case of linearly polarized light.

The photoisomerization of azobenzene is a complex quantum mechanical phenomenon which involves excitation of the electrons of the N=N double bond, and takes place on the time-scale of tens of picoseconds (Michl and Thulstrup 1995).

However, given the scale of the force-field modeling employed here, one can reduce it to the same classical mechanical level. It is assumed here that the material contains azobenzene chromophores with such chemical substituents (e.g. NO_2) that continuous *trans-cis-trans* isomerization cycles occur at a certain wavelength of the illumination. Given that the rate of the *trans-cis* photoisomerization is proportional to $\cos^2\theta_i$ (θ_i is the angle between the long axis of the i-th *trans*-isomer and the light polarization), the *trans*-isomers are to be found predominantly perpendicular to the light polarization (orientational hole-burning effect). On the classical mechanical level this effect can be modeled by introducing a reorienting field which acts on each *trans*-isomer. The corresponding energy reads:

$$U_i^{\text{azofield}}(\theta_i) = F \cdot P_2(\cos\theta_i). \tag{4.14}$$

Here the field strength is $F > 0$ (again we will use the reduced field strength, f, where $F = f \cdot 10^{-20}$ J), θ_i is the angle between the long axis of the i-th *trans*-azobenzene and the direction of the field, and $P_2(x)$ is the second Legendre polynomial. The derivative of $U_i^{\text{azofield}}(\theta_i)$ with respect to θ_i is related to the torque acting on the i-th azobenzene. One should note that, while both electric and magnetic fields align the azobenzenes uniaxially [this corresponds to Eq. (4.10) with $f > 0$], the model field defined via Eq. (4.14) with $f > 0$ forces azobenzenes to stay preferentially in the plane perpendicular to the field direction. The latter can be associated with the polarization of the beam.

The aim of this study is to find the most relevant mechanisms for the photo-induced deformations and, therefore, some aspects of the photoisomerization are not considered. These are, in particular, the presence of *cis*-isomers and the kinetics of the photostationary state. The only effect being taken into account is the reorientation of the *trans*-isomers of the azobenzenes when the material approaches the photostationary state. Throughout this study, however, we discuss the possible relevance of the *cis*-isomers in each particular case.

4.2.1 Modelling of Photo-Induced Deformations in Weakly Coupled SCLCP

We consider the SCLCP in a weak coupling limit represented by exactly the same model as in Sect. 4.1. A monodomain smectic volume element, obtained with the aid of aligning field (4.10) is well equilibrated at $T = 485$K, which is just below $T_{\text{SI}} \sim 490$K (Ilnytskyi and Neher 2007). The azobenzene director is collinear with the Z axis, and initial values for both order parameters are equal: $S_{\parallel} = S_2 \approx 0.75$. In the absence of an external field the phase is stable for at least 120 ns with minimal fluctuations of the order parameters and of the box dimensions. With application of the field along the nematic director, this arrangement becomes energetically unfavorable and a torque applied to each chromophore attempts to reorient it

perpendicularly to the field. The rate of the reorientation depends on the field strength f, but is also affected by coupling of the chromophores to the polymer matrix.

What kind of response of the polymer matrix can be expected? If the field is strong enough (large f), then the time scale of chromophore reorientation may become much shorter than typical relaxation times of the polymer matrix. In this case one, generally, expects development of the internal stress and deformation of the volume element. At small values of field strength f, the time scales of both processes may become of the same order. Then, one may expect several scenarios: (a) reorientation of azobenzenes with no deformation of the polymer (due to stress relaxation); (b) monotonical deformation of the polymer over an extended time interval, "in phase" with reorientation of chromophores; or (c) deformation of the polymer on a similar time scale as for the moderately strong field case (phase-transition-like changes).

We found only two scenarios. At field strengths of $f = 0.015$–0.020, the typical "weak field scenario" with the SI transition was observed [see results averaged over this interval marked (b) in Fig. 4.6]. Unfortunately, these particular simulation runs cannot be prolonged due to the effect of "monolayering" of the simulation box, in which case the simulations are terminated. The reason behind this shortcoming is that the $NP_{xx}P_{yy}P_{zz}T$ ensemble is not well suited for the simulation of isotropic phases, where random fluctuations of the simulation box dimensions take place (Allen and Tildesley 1989). The run with a very weak field, $f = 0.005$, turned out to be unaffected by this problem for more than 120 ns [curves (a) in Fig. 4.6]. The SI phase transition takes place during the time interval $t \sim 45$–65 ns, after which no apparent changes are observed for about 45 ns in the smectic phase, but the duration of the transition (approximately 20 ns) is the same as for the

Fig. 4.6 Field-induced changes in the order parameters of azobenzenes, $S_{\parallel}$ (*top frame*), and in the strain along the field, $\varepsilon_{\parallel}$ (*bottom frame*), for the monodomain smectic phase at $T = 485$K. (*a*) $f = 0.005$; (*b*) average over $f = 0.015$, $f = 0.017$ and $f = 0.020$ runs; (*c*) average over $f = 0.1$ and $f = 0.16$ runs. Reprinted with permission from Ilnytskyi et al. (2011). Copyright 2011, AIP Publishing LLC
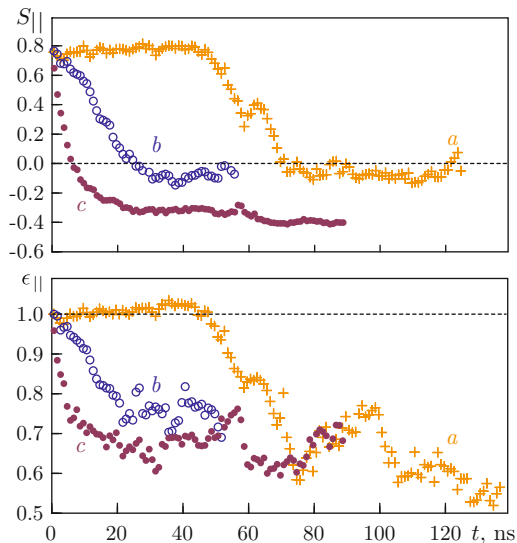
case of higher field strengths $f = 0.015$–0.020. Therefore, fourfold reduction of the field strength has the effect of merely time shifting the transition, but not changing its typical time scale.

The SI transition is accompanied by an essential contraction of the simulation box along the direction of the field (see the curves for the strain $\varepsilon_\parallel$ in Fig. 4.6, curve a). We can conclude that, at least within a time window of 120 ns, we hit some interval of field strengths f for which the SI transition can be achieved solely due to the reorientation of *trans*-azobenzenes [with no formation of *cis*-isomers, as in the case of the real photo-chemical transition (Ikeda et al. 1990, 2002; Ikeda 2003; Barrett et al. 2007)]. Deformation of the box can be explained by the following considerations. The duration of the SI transition is about 20 ns (the time interval $t \sim 45$–65 ns in Fig. 4.6), and it is shorter than the estimated relaxation times for the chromophore reorientations in the equilibrium state, $\tau \approx 43$ ns (Ilnytskyi and Neher 2007). As a result, the polymer is not given enough time to relax during the transition, and deformation of the polymer matrix takes place. The synchronicity in changes of $S_\parallel$ and $\varepsilon_\parallel$, clearly seen in Fig. 4.6, indicates a strong coupling between the amount of the orientational order of the mesogens and the shape of the simulation box.

With the increase of f beyond $f \sim 0.020$ one observes the "strong field" scenario, in which two processes take place (see curves c in Fig. 4.6). The first process is the SI transition which occurs for $t < t^* \approx 5$ns. It is followed by the second process, for $t > t^*$, during which the smectic phase is regrown with its director now being perpendicular to the field [relevant snapshots can be found elsewhere (Ilnytskyi et al. 2006)]. Typical time scales of these transitions depend on the strength of the field; the data averaged over $f = 0.1$ and $f = 0.16$ runs are shown in Fig. 4.6 (curve c). One can conclude that in the first process the field acts as a "melter" of the smectic phase and in the second as an aid for the self-assembly of the isotropic melt into the smectic phase. In this way, the "strong field" scenario combines both effects of the photo-induced order–disorder transition and of the photo-alignment in azo-polymers (Ichimura 2000; Ikeda et al. 2002; Ikeda 2003). Generally speaking, during the field-aided self-assembly the possibility of the planar phase exists, in which chromophore orientations are confined within the planes (perpendicular to the direction of the field) but with no orientational order within the planes. However, this phase is observed in none of the simulations being performed. The in-plane 2D symmetry is always broken in favour of the smectic layers. This is in agreement with predictions of the thermodynamic theory developed recently for LC azobenzene elastomers (Toshchevikov et al. 2012; Toshchevikov and Saphiannikova 2014).

One should stress that, for the "strong field" scenario, the anisotropic deformation of a volume element occurs only during the first process ($t < t^*$, SI transition), where $\varepsilon_\parallel$ decreases significantly. The second process, for ($t > t^*$, isotropic–smectic transition), takes place with no apparent systematic changes in the box dimensions. Therefore, the contraction of the volume element is reported for our model for both "weak field" and "strong field" scenarios. We can deduce that contraction of the smectic monodomain sample along the field is achieved primarily due to the destruction of the initial smectic order.

One may conclude that the defining factor in contraction of the volume element along the field is the "randomization" of the azobenzene orientations. The spacers are also known to align partially along the nematic director in the smectic phase (Ilnytskyi and Neher 2007); therefore these also add to the net effect. The contribution from the rearrangements of the backbones is also present in the deformation of the volume element observed as the result of the simulations. However, due to their flexibility, their effect is minor (Ilnytskyi et al. 2011).

4.2.2   Modelling of Photo-Induced Deformations in Strongly Coupled SCLCP

The strongly-coupled model is used to simulate photo-induced deformations in amorphous azo-polymers. The properties of this model, and the estimate for the glass transition temperature, have been discussed in the relevant part of Sect. 4.1.

Most SRG inscriptions in amorphous systems are performed at $T < T_g$, aimed at fabrication of technologically desirable long-term stable gratings. However, even the changes in the inscription process when one approaches T_g may shed much light on the tendencies of the relevant mechanisms at still lower temperatures. It was shown in recent experiments (Veer et al. 2008, 2009) that under continuous exposure the grating height decays exponentially with the temperature increase, and no permanent SRG can be recorded if $T > T_g - 20\,°C$. However, under pulse-like exposure, the grating still exists as long as the actinic light is on. It follows that at $T \sim T_g$ the SRG can be stable over a short time interval, whereas subsequent stress relaxation prevents formation of a permanent grating.

We perform MD simulations both above T_g and at $T \sim T_g$. All results presented in this section are obtained on macroscopically isotropic volume elements. Three simulations were undertaken at each field strength f (the field in each case was directed along the X, Y and Z axes, respectively) and the results were averaged over these three runs. In this way, we attempt to exclude the possibility that the effects being observed are related to the fluctuations. This also mimics some minimal sample averaging, combined with the averaging over the runs with close values of f.

Let us first discuss the results obtained at $T = 500K > T_g$, where the melt has viscoelastic properties. Photo-induced deformations take place within a certain interval of field strengths: $f = 1$–1.7. Here we will restrict our discussion to the single case of $f = 1.6$. The field is switched on at $t = 0$ and switched off at $t = 24ns$. The evolution of the order parameter along the field $S_\parallel$ (shown separately for the backbones and mesogens), and the photo-induced strain $\varepsilon_\parallel$, are presented in the two left frames of Fig. 4.7.

Similarly to the case of the weakly-coupled model, considered in the previous section, the effect of photo-induced reorientation of chromophores is observed clearly. The changes in the order parameter of the backbones are found to take place on the same time scale; this indicates the reorientation of the molecule as a
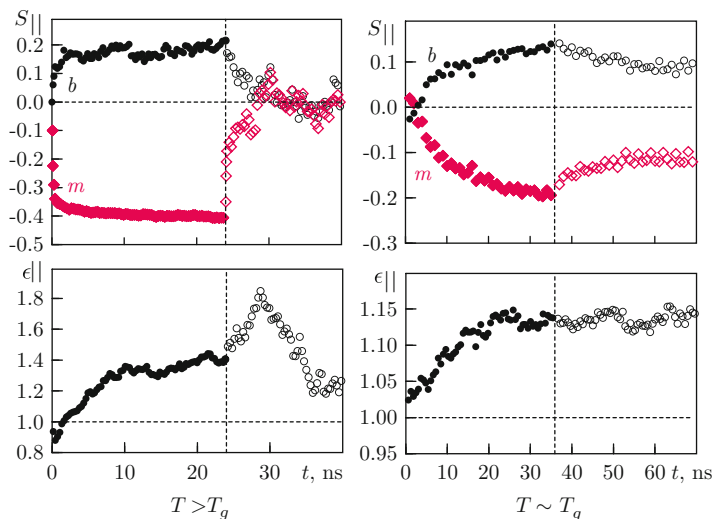
Fig. 4.7 Evolution of the order parameter $S_\parallel$, and the photo-induced strain $\varepsilon_\parallel$, along the external field (shown in *solid symbols*) and after the field is switched off (*open symbols*). The values of $S_\parallel$ for both the backbones (*b*) and the mesogens (*m*) are indicated. *Left frames* show the case $T = 500$ K $> T_g$ at field strength $f = 1.6$. *Right frames* show the case $T = 450$K $\sim T_g$, for which the data is averaged over the results for $f = 0.15$, 0.20 and 0.50. Reprinted with permission from Ilnytskyi et al. (2011). Copyright 2011, AIP Publishing LLC

whole (due to the strong coupling nature of this molecular architecture). The effect of backbone stretch is also present, but it is relatively weak (Ilnytskyi et al. 2011).

It is very important to note that the same principal structural changes (reorientation of the chromophores and backbones perpendicularly and parallel to the field, respectively) are observed as in the case of the weakly-coupled SCLCP azo-polymer. However, the mechanical response of the strongly-coupled system is the opposite: the volume element extends about 140 % along the field (Fig. 4.7, bottom frame). As far as the backbone reorientation contributes to the volume element expansion, one can conclude that this effect is more essential than the reorientation of chromophores. The result can be attributed to backbone stiffness and to a short spacer, which helps to transfer any torque imposed on the chromophores straight to the backbones.

The changes are, however, reversible. After the field is switched off at time $t = 24$ns, within 10–15 ns the field-induced state of the polymer reverts back to almost the initial state. In particular, the order parameter of backbones along the field $S_\parallel$ decreases, and the strain of the volume element in the same direction $\varepsilon_\parallel$ changes back towards the initial value. This mimics the experimental findings on impermanent SRGs if performed in amorphous materials that are not deep enough in a glassy state (Veer et al. 2008, 2009). The analysis of the model structure formed under the field, which corresponds to the time interval $t = 20$–24 ns, reveals that it is a polydomain one with strong local liquid crystallinity (Ilnytskyi et al. 2011).

The field effectively drives the system to a state with similar structure as is observed at and below its glass transition temperature T_g. After the field is switched off, the system recovers the structure it had at $T > T_g$.

Most SRGs are recorded deep below T_g; typical recording times for amorphous systems range from seconds to days. Such time scales are inaccessible for semi-atomistic simulations. Therefore, we limit our analysis to the tendencies undergone by the process of photo-induced deformations when one approaches the glass transition temperature. These could be extrapolated further to the $T < T_g$ region. Therefore, the simulations are performed at $T = 450K \sim T_g$, where the estimate for $T_g \approx 445K$ is based on Fig. 4.4. A well equilibrated configuration was prepared by cooling the melt from $T = 500K$ down to $T = 450K$ and by subsequent equilibration for a relatively long time of 65 ns. Similarly to the case of $T = 500K$, an external field was applied in turn along each spatial axis and the results were averaged over the three runs. The effect of photo-induced deformation was observed in the range of $f \sim 0.1$–0.7, and these values are essentially lower than $f \sim 1$ required in the case of $T = 500K$.

All properties of interest are found to behave quite similarly for field strengths $f = 0.15$, 0.20 and 0.50 (here one can ignore small differences in reorientation dynamics in this interval of values of f), and, therefore, the results are averaged over these runs to improve statistics. The data is shown in the right frames of Fig. 4.7. The changes in orientational order parameters for chromophores and backbones, acquired due to application of the field, are found to be stable after the field is switched off (at $t = 37ns$) for at least another 30ns. This is in a sharp contrast to the case of $T = 500K$, when the order vanishes in about 5 ns after the field is switched off. The same holds true also for the strain of the volume element along the field, $\varepsilon_\parallel$, which is found to behave smoothly with no "kick" after the field is switched off. The expansion of the box acquired along the applied field is preserved for at least another 30 ns after the field is switched off. More precise determination of the stability of field-induced deformation requires much longer simulation runs which, in turn, needs a simulation box of a larger size. The reason for this is that the film can turn into a monolayer in one of the dimensions perpendicular to the field, due to spontaneous shape fluctuations.

Let us consider again the possible role of the *cis*-isomers, which have not been taken into account explicitly here. Their presence will dilute, and, therefore, lessen the local LC ordering and decrease the role of physical crosslinks, the effect that prevents mechanical changes at higher values of field f. Otherwise, the *cis*-isomers will decrease the net torque applied on each molecule, which may result in a need for stronger fields to be applied or longer time to achieve the deformation. In any case, the same basic mechanism is expected to hold.

The results obtained at both $T > T_g$ and $T \sim T_g$ provide evidence for the following microscopic mechanism for photo-induced deformations in a strongly-coupled model SCLCP. First of all, due to the strong coupling between chromophores and backbones, the molecules behave similarly to rigid bodies (the time scale of the order parameter evolution for both chromophores and backbones is the same). Given suitable conditions, these massive molecular reorientations lead to the

build-up of anisotropic internal stress, which causes temporary or permanent deformation of the volume element. In the case of $T > T_g$ the deformation is observed at moderately large field strengths, $f = 1$–2, in which case the system is driven first to the state with higher density (typical for the temperature range $T < T_g$). The deformations are temporal, inasmuch as, upon switching the field off, the system reverts back to almost the initial (pre-field) state. In the case of temperatures $T \sim T_g$, the initial density of the melt is essentially higher and the internal stress (and, consequently, anisotropic deformation) is developed at much weaker fields, $f = 0.1$–0.7, and stays permanent during at least the simulation time of 30 ns performed in this study. The sign of the deformation (extension of the volume element along the field direction) highlights the role of backbone rigidity, in that the effect of backbone reorientation wins over the effect of chromophore reorientation perpendicularly to the field.

4.3 Elasticity and Memory Effects in SCLCE

4.3.1 Preparation of the Elastomer and Shift of the Smectic-Isotropic Transition

As already discussed above, the elastomer matrix acquires some new properties as compared to the case of the melt. Specifically, the viscosity of the polymer subsystem is suppressed in favor of elasticity. The latter provides the reversibility of the system response when it is perturbed via some external stimulus. Modeling of these effects is the subject of the current section.

The SCLCE is prepared by crosslinking the SCLCP melt, which is equilibrated in the smectic phase. For this purpose we used the model depicted in Fig. 4.1 and described in detail in Sect. 4.1. The following parameters are used: $L_b = 100$, $L_c = 6$ and $k_f = 2$. Out of $N_c = 50$ pendant side chains, 40 are terminated by a mesogen, whereas the remaining 10 are terminated by chemically active particles, which can form crosslinks. Both backbone and side chains are chosen to be flexible, with appropriate parameters $\{C_i\}$ for the torsional potential V_t, discussed in detail in Sect. 4.1. The smectic phase was prepared with the aid of the aligning field of Eq. (4.10), as described above for the case of the weakly-coupled limit.

To avoid disruption of the initial smectic structure of the melt, we opted to use "rubber band" crosslinks of about 4Å in length that are longer than true "chemical" bond lengths (e.g. ~ 1.54Å for hydrocarbons) instead of forcing reactive sites into closer contact. $N_{cl} = N_{mol} = 28$ crosslinks are made using an algorithm which attempts to crosslink homogeneously through the simulation box; more details are given elsewhere (Ilnytskyi et al. 2012).

One can classify the effects observed in LCEs under external stimuli on the basis of the physical nature of the latter. Let us start from the effects connected with temperature change. For weakly crosslinked networks, the LC groups retain the

ability to form LC phases, and the LC transitions are the only principal changes undergone by LCEs on varying the temperature (presuming the temperatures to lie above the glass transition temperature). Crosslinking stabilizes the LC phase in which the network is originally formed, due to memorizing the backbone conformations (Symons et al. 1993, 1999; Davis and Mitchell 1996; Warner et al. 1988). This is indicated by a rise of the order–disorder transition temperature, if crosslinking was performed in an ordered phase. The exact amount of the shift of the transition temperature depends on crosslink density, the level of nematic order, and other factors (Symons et al. 1999) but is, typically, a few degrees for weakly crosslinked LCEs. One, however, needs to take into account that, in contrast to low-molecular-weight LC materials, the order–disorder phase transition in LCEs is more smeared. The isotropic–nematic coexistence over a broad temperature range suggests that the heterogeneity in the samples introduces a distribution of transition temperatures (Zhang et al. 2006). Therefore, one might refer rather to a certain "transition region", which defines an approximate interval for the SI transition temperature, T_{SI}. This interval is estimated from a series of heating runs performed at a range of temperatures, each run started from the same smectic sample being equilibrated at 450 K for at least 10 ns. The evolution of the order parameter S_2 is shown in Fig. 4.8 for both cases of LCP melt and LCE. The transition region is found to be 500–505 K for the melt and 505–510 K for the elastomer, respectively. Therefore, the estimated increase of the transition temperature due to crosslinking of the melt is $\sim 5\,^\circ$C, in agreement with typical experimental findings (Symons et al. 1993, 1999; Davis and Mitchell 1996; Warner et al. 1988).

Fig. 4.8 *Top row*: evolution of the nematic order parameter for the LC groups in the LCP melt (*left frame*) and in the LCE (*right frame*) upon heating the initial smectic sample equilibrated at $T = 450$K up to higher temperatures indicated in the *left frame* of the plot. *Bottom row*: the same for the uniaxial strain of the sample $\varepsilon_\parallel$ along the initial nematic director. Adapted from Ilnytskyi et al. (2012) with permission from The Royal Society of Chemistry
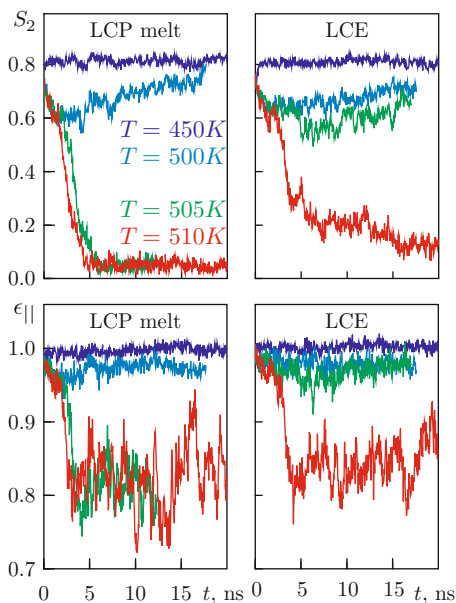
It is well known from the experiments that the change of LC order is accompanied by deformation of the material along the director axis (Schätzle et al. 1989; Assfalg and Finkelmann 1989; Tajbakhsh and Terentjev 2001; Hirschmann et al. 2001; Cladis 2001; Warner and Terentjev 2003). A wide range of strain values have been observed, from 0.29 (Tajbakhsh and Terentjev 2001) to 0.95 (Mitchell et al. 1993; Hirschmann et al. 2001). The amount of strain depends on the coupling between the average anisotropy of polymer chains and the nematic order parameter, and it has some specific features outlined below. Small-angle neutron scattering experiments on deuterium labeled mixtures have revealed that both types of backbone anisotropy, parallel and perpendicular to the director, are possible (Mitchell et al. 1991; Kirste and Ohm 1985; Keller et al. 1985), as well as switching between the two (reminiscent of the odd-even effect in nematics) (Mitchell et al. 1992). In this respect, positive and negative coupling coefficients are often used indicating that backbones are extended parallel or normal to the liquid crystal director, respectively. As remarked in Küpfer and Finkelmann (1991), for nematic polymers, typical ratios between radii of gyration of backbones parallel and perpendicular to the director, $R_{\parallel}/R_{\perp}$, are found close to 0.7 or 1.3. For smectic polymers, backbones are confined inside layers and $R_{\parallel}/R_{\perp}$ is much smaller than one (Ilnytskyi and Neher 2007).

This effect is also reproduced in our simulation, evidenced by the behavior of a uniaxial strain $\varepsilon_{\parallel}$ along the axis of the initial director; see relevant frames of Fig. 4.8. In the case of our model, the backbone is flexible and the coupling between the nematic director and backbones is negative; thus both compete in influencing the shape of the sample. However, as in the case of the similar weakly-coupled model with different values for L_b, L_c and k_f, discussed in Sect. 4.2, the sample contracts when driven through the SI transition. This, presumably, can be attributed to the flexibility of the model backbone in both cases. It is important to note that the transition-induced strain is weakly dependent on whether the crosslinking is performed or not. In both cases of melt and network, it is of the order of 0.8, see Fig. 4.8. However, despite much similarity between the cases of LCP melt and LCE in terms of deformation upon entering the isotropic phase, both systems demonstrate quite different attitudes towards the shape memory effects. This is considered in detail in the following section.

4.3.2 Memory Effects

Due to coupling between the LC and polymer subsystems, LCEs display a number of reversible opto- and thermo-mechanical effects, which brings them into the wider class of shape-memory polymers (Behl and Lendlein 2007; Ahn et al. 2011). In particular, the sample may be held at temperatures well above the nematic–isotropic transition for extended periods (2 weeks), but on cooling into the LC phase region, the original monodomain order is recovered with the same director alignment (Legge et al. 1991). This is in contrast to the case of an uncrosslinked sample of the same copolymer, in which case no retention of the global orientation was

shown after holding the sample for 60 s in the isotropic state (Legge et al. 1991). These thermo-mechanical memory effects, observed experimentally (Legge et al. 1991; Mitchell et al. 1993), form a basis for possible technological applications of LCEs as artificial muscles (Shenoy et al. 2002; Spillmann et al. 2007).

We aim to reproduce, by simulation, the reversibility of the orientational order, and of the sample shape, when the LCE is driven on a temperature scale back and forth through the order–disorder transition. To this end, we performed a set of runs started from the initial smectic phase that is equilibrated at 450 K. This phase is subjected to annealing at 510 K. During the process, we picked samples annealed for 4, 12, 20 and 28 ns and performed their quench at $T = 450$K for at least 20 ns. The main question is whether or not this quenching will revert the structure to the initial smectic phase. The answer is *no* for the case of the LCP melt [the plots are given elsewhere (Ilnytskyi et al. 2012) and are not repeated here]. However, for the case of the LCE, complete reversibility of the structure is observed at least within a time window 40 ns of our simulations. In particular, the behavior of the mesogen order parameter S_2, as evidenced in Fig. 4.9, indicates that the LC subsystem self-assembles back into the smectic phase as the result of quenching. The evolution of the uniaxial strain $\varepsilon_{\parallel}$ along the axis of the initial nematic director is also shown in Fig. 4.9. The initial strain fully recovers for all quenching runs performed. The evolution of the order parameter, and that of the strain upon quenching, are found to
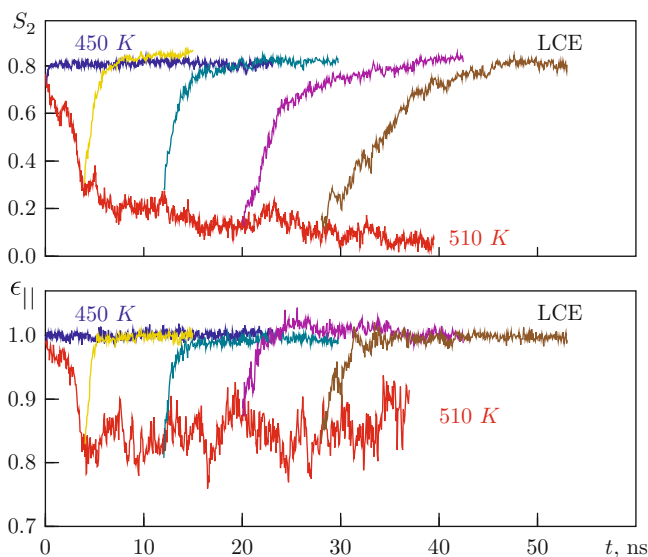
Fig. 4.9 *Top frame*: nematic order parameter S_2, *bottom frame*: uniaxial strain $\varepsilon_{\parallel}$ along the axis of the initial nematic director during annealing-quenching runs of LCE. The initial structure is well equilibrated at 450 K in the smectic phase (*blue curve*). An annealing run is performed at $T = 510$ K (*red curve*) and quenching runs are performed back to $T = 450$K (*other colors*) for the structures partly annealed for 4, 12, 20 and 28 ns. Adapted from Ilnytskyi et al. (2012) with permission from The Royal Society of Chemistry
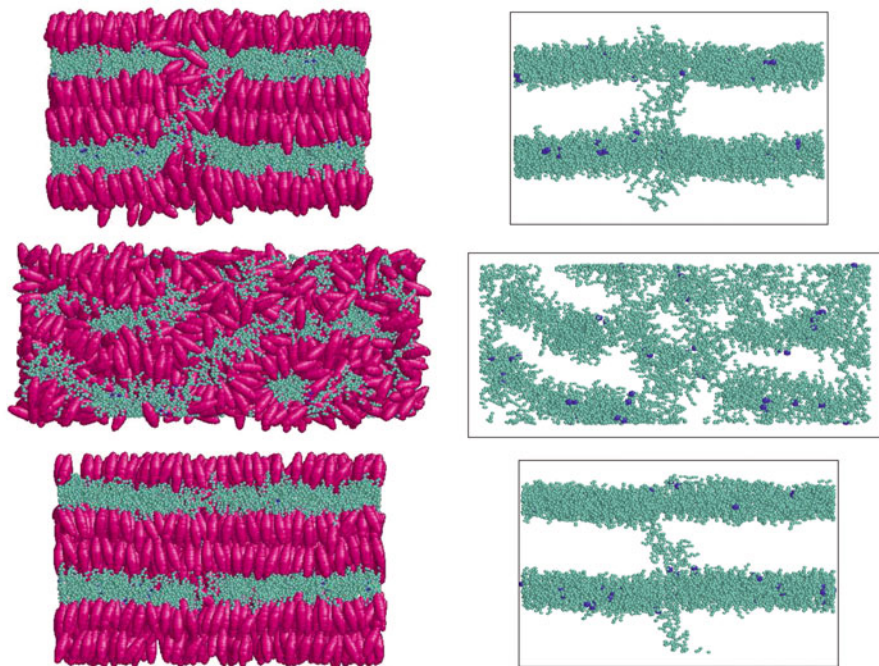
Fig. 4.10 *Top row*: snapshots for the initial smectic phase at $t = 0$. *Middle row*: structure partly annealed at 510 K for 20 ns. *Bottom row*: recovered smectic structure as the result of quenching back to 450 K. Snapshots showing both polymer and mesogens are on the *left*, snapshots showing backbones only are on the *right*. Reproduced from Ilnytskyi et al. (2012) with permission from The Royal Society of Chemistry

be fully synchronized. Visual representation of this memory effect is provided in Fig. 4.10, where snapshots are given for the initial structure, partly annealed structure after 20 ns, and recovered structure.

The reversibility of the smectic structure upon annealing/quenching runs in the LCE case can be interpreted by hampering the diffusion via crosslinking. As one can see from Fig. 4.10, the partly annealed structure preserves the essentials of the layered structure of the initial phase, despite the layers being bent and distorted. This memory effect of the polymer matrix plays the principal role in a quick rebuild of an exact replica of the initial smectic structure.

4.3.3 Stress-Driven Effects in the Isotropic and Smectic Phases

Let us switch now to the opposite type of effect, in which a mechanical load is used as a driving stimulus. It has been known since the early studies that in this way one can manipulate the LC order of the LCE (Finkelmann et al. 1981, 1984; Mitchell

et al. 1987; Degert et al. 1992). A fundamental mechanism here is that an applied stress induces an anisotropy in the polymer backbone, which results in a macroscopic alignment of the director by virtue of coupling (Hirschmann et al. 2001). Due to this, the load induces remarkable changes in the structure of the LCE, if its axis is not collinear with the axis of initial anisotropy of backbones.

When applied to a globally isotropic sample, a uniaxial load is able to induce homogeneous LC order. This effect is used for fabrication of liquid single crystal elastomers via a two-stage crosslinking technique (Küpfer and Finkelmann 1991). On the other hand, when applied to an initially ordered monodomain nematic LCE, the load may change the already-existing LC order (Finkelmann et al. 1981; Küpfer and Finkelmann 1991; Mitchell et al. 1993). In the case of positive LC-backbone coupling, the changes occur when the load axis is not collinear with the initial director, due to the arguments above. When the load is applied normally to the director, then the sample first turns opaque (accompanied by softening of the material) and then a monodomain sample is formed in which the director is parallel to the load (Küpfer and Finkelmann 1991). The opaque state turns out to have a periodic V-shaped pattern. When the strain is applied nearly normal to the initial director, molecular rearrangement is accompanied by a decrease in nematic order parameter during the rotation (Roberts et al. 1997). Wide-angle X-ray scattering and optical microscopy studies have revealed a single director orientation throughout the switching process; broad optical-texture variations are observed after the director flip has occurred, although the sample remains optically clear throughout the process (Roberts et al. 1997). Director reorientation in nematic LCEs is also extensively discussed theoretically (Verwey et al. 1996; Warner and Terentjev 1996; Bladon et al. 1993, 1994; Weilepp and Brand 1996).

Much less work has been done on smectic-A elastomers. It was found (Nishikawa et al. 1997) that macroscopically uniformly aligned smectic-A LCEs are characterized by a highly anisotropic solid-like response, with an elastic constant along the layer normal about two orders of magnitude larger than that in the layer plane. When the sample is deformed parallel to the layers, it responds as a two-dimensional elastic network: the sample stays clear up to high strains of 200 %, and maintains its full width in the direction parallel to the layer normal (Nishikawa et al. 1997). However, when the sample is stretched along the layer normal (parallel to the director), stress-driven changes in the LC order are observed, due to negative backbone-LC coupling. If the load is applied in this way, and it exceeds a threshold value, then a breakdown of the monodomain structure is observed, resulting in a completely turbid sample (Nishikawa et al. 1997) suggesting layer undulation (see Fig. 14 in Nishikawa and Finkelmann 1999). This turbidity is the result of textured deformations that are formed as a response on a macroscopically homogenous strain (Biggins 2009; Kundler and Finkelmann 1995, 1998).

This behavior can be explained as follows. When the LCE is stretched and the nematic director rotates, the energy of the deformation is much reduced if the elastomer also shears. The sample is split into stripes that alternate between equal and opposite director rotation and shear (Verwey et al. 1996; Finkelmann et al. 1997; Biggins 2009). This scenario is especially true for smectic LCEs, that

are layered, and there is a large energy penalty associated with causing the director to deviate from the smectic layer normal, or changing the inter-layer spacing (Adams and Warner 2005). The uniform director rotation *vs* patterned stripes scenario, when the LCE is stretched perpendicularly to the director, may also depend on the details of sample preparation (Zhang et al. 2006).

To model these experimental effects, we simulated a creep experiment, and compared the output depending on the sample phase and whether or not it is crosslinked. The results for the mechanical properties in terms of the evolution of the strain parallel ($\varepsilon_\parallel$) and perpendicular ($\varepsilon_\perp$) to the load axis during a creep are collected in Fig. 4.11. In the case of the isotropic phase, the LCP melt behaves in a purely viscous manner: $\varepsilon_\parallel$ increases sharply until the sample fractures (indicated by "$\times$" symbols), see curves marked as "LCP melt" in Fig. 4.11a. On the contrary, the isotropic phase of the LCE (prepared by heating up and equilibrating the smectic at $T = 510$K) demonstrates a viscoelastic behavior. In particular, the sample has a viscous regime for $t < t^* \sim 20$ns, whereas for $t > t^*$ it displays elasticity, in which case $\varepsilon_\parallel$ saturates. In the latter regime, the sample withstands a load of at least 37atm, see the same plot, curves marked as "LCE". The changes in the structure of the sample under load will be considered below.

The creep of the smectic LCP melt leads to very similar results when the load is applied along or perpendicular to the nematic director. The former case is shown in Fig. 4.11b. Contrary to the case of the isotropic LCP melt, a plateau in $\varepsilon_\parallel$ exists at the start of the creep, where the sample keeps its shape, but accumulates small structural changes. The latter then lead to the disintegration of the sample, very similar to the case of the isotropic LCP melt (Fig. 4.11a, curves marked as "LCP melt"). The smectic LCP melt, therefore, behaves as a "soft solid".
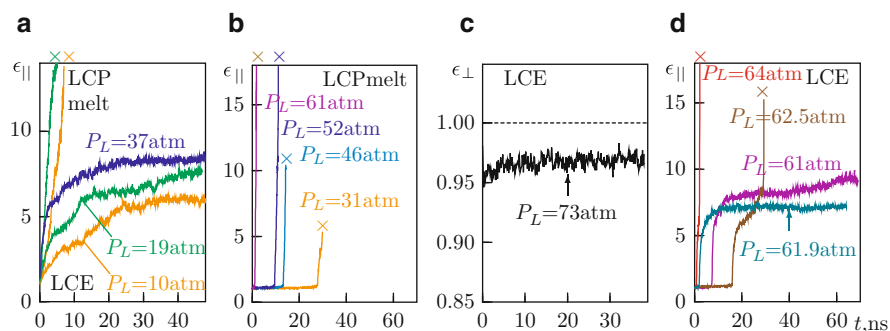
Fig. 4.11 Evolution of a uniaxial strain parallel ($\varepsilon_\parallel$) or perpendicular ($\varepsilon_\perp$) to the load axis during the simulation of a creep experiment of LCP and LCE in different phases. Amount of applied load P_L is shown in each case; *cross-symbols* indicate fracturing of the sample. (**a**) Isotropic phase, both cases of LCP melt and LCE are combined and marked in one plot. (**b**) Smectic phase, LCP melt, load axis is collinear with nematic director. (**c**) Smectic phase, LCE, load axis is perpendicular to nematic director; $\varepsilon_\perp$ (which is collinear with the director) is shown. (**d**) Smectic phase, LCE, load axis is collinear with nematic director. Adapted from Ilnytskyi et al. (2012) with permission from The Royal Society of Chemistry

The behavior of the smectic LCE under creep is essentially anisotropic and closely follows that of real systems, discussed above. First we simulated a creep experiment with a load $P_L = 73$atm applied perpendicular to the nematic director (e.g. along the Y axis). The load axis in this case is located within the 2D layers of the crosslinked polymer, as seen in Fig. 4.10. The network is found to stretch along the axis of load by 230 %, but displays remarkably little deformation along the axis of the nematic director, as monitored by the behavior of $\varepsilon_\perp$ in that direction, see Fig. 4.11c. The case when the load is applied parallel to the director is shown in Fig. 4.11d. Here we have observed several regimes exhibited in the previous cases. Namely, at moderate load $P_L \leq 62$atm there are: (i) an initial "solid-like" regime with constant strain, where the smectic phase withstands the load; (ii) a transition-like shape transformation, when the deformation along the load, $\varepsilon_\parallel$, rapidly increases; and (iii) a plateau-like region, where the sample is kept by elastic forces. At higher load, $P_L > 62$atm, the sample behavior is dominated by the fourth regime, (iv) disintegration.

To clarify the origin of the transition-like shape transformation denoted as (ii) above, we focus on properties that characterize the microscopic state of the backbones and mesogens. The level of backbone stretch along the axis of the load is characterized by the ratio $R_\parallel/R_\perp$ between the two components of the radius of gyration, respectively along and perpendicular to the load. The anisotropy of orientational order of mesogens with respect to the load axis is characterized by the respective order parameters $S_\parallel$ and $S_\perp$. Due to rapid disintegration of both isotropic and smectic LCP melts, we limit our study to the LCE case only.

The results for the isotropic LCE are shown in Fig. 4.12a. One can observe that in the viscous regime $t < t^*$ the backbone anisotropy increases sharply. At the end
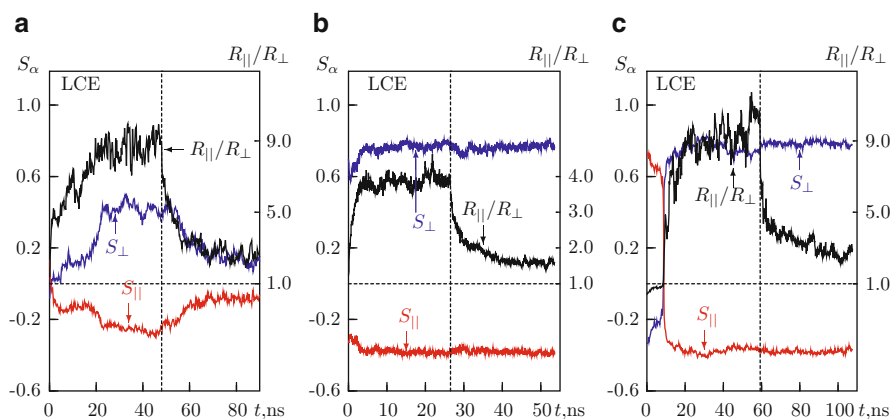
Fig. 4.12 Gyration radius anisotropy $R_\parallel/R_\perp$ for the backbones, and orientational order parameters $S_\parallel$ and $S_\perp$ for the mesogens, with respect to the direction of uniaxial load. (**a**) Isotropic phase. (**b**) Smectic phase, load axis is perpendicular to the nematic director. (**c**) Smectic phase, load axis is parallel to the nematic director. Adapted from Ilnytskyi et al. (2012) with permission from The Royal Society of Chemistry
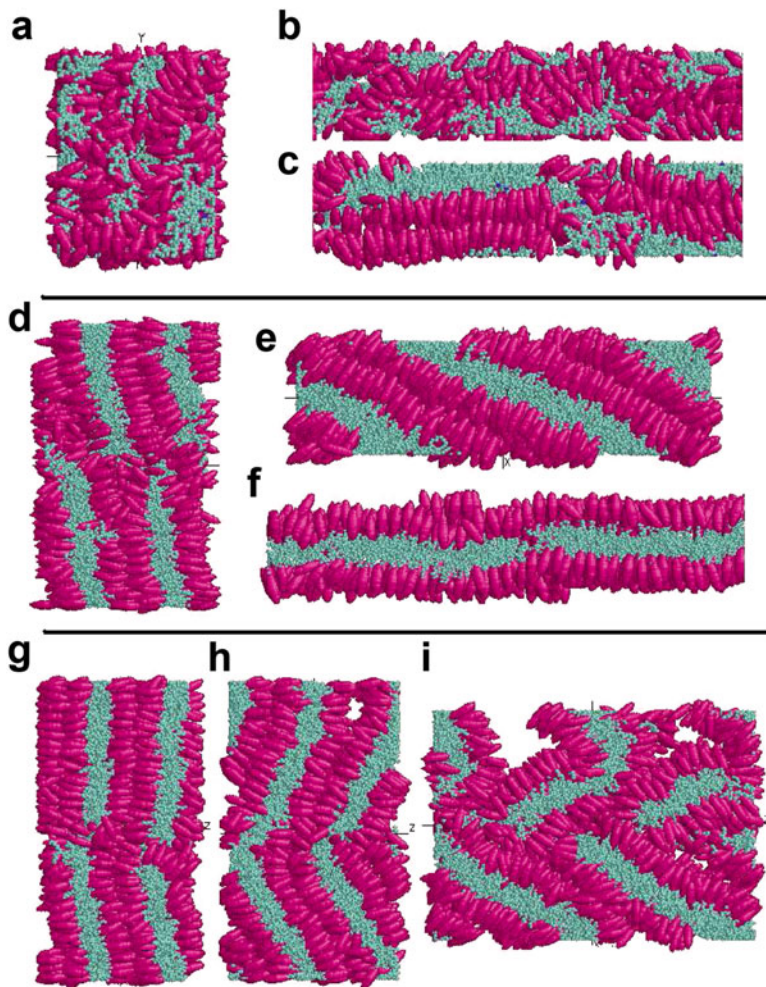
Fig. 4.13 Snapshots illustrating the structural changes of the LCE upon application of an external uniaxial load. (**a**, **b**, **c**) Isotropic phase at $T = 510$K being under load of $P_L = 37$atm for 0, 16 ns and 48 ns, respectively. (**d**, **e**, **f**) Sample 1 of smectic phase at $T = 480$K being under load of $P_L = 73$ atm for 0, 8.8 ns and 31.8 ns, respectively. (**g**, **h**, **i**) Sample 2 of smectic phase at the same temperature and load as the previous one, being under load for 0, 1.6 ns and 1.88 ns, respectively. Adapted from Ilnytskyi et al. (2012) with permission from The Royal Society of Chemistry

of this regime the mesogens follow the spatial redistribution of the backbones indicated by the increase of their order parameter $S_\perp$. The formation of this stress-induced ordered phase is displayed in Fig. 4.13, frames a–c. One can deduce that, for the negative coupling between the two subsystems to work, and for the ordered phase to form, considerable backbone anisotropy of at least 5–6 is required. On release of the stress, the backbones ordering moves back towards the pre-deformational initial state, but a residual backbone anisotropy of about 2.5–3,

and residual order of $S_y = 0.15$, are still preserved 40 ns after the load was released, see Fig. 4.12a.

For the case of the smectic LCE, as follows from the discussion of the experimental results above, the existing LC order can be changed or remain intact when a uniaxial load is applied. The result depends on the choice of the load axis. On a par with the experimental findings, we found that when the load is applied perpendicular to the director in our model SCLCE, it has no effect on the mesogen order. This is clearly seen in Fig. 4.12b. While the $R_{\parallel}/R_{\perp}$ ratio changes, essentially following the load, only negligible changes are observed for the order parameters $S_{\parallel}$ and $S_{\perp}$. The polymer and mesogen subsystems appear to be completely decoupled. The survival of smectic layers is evidenced also by virtually no change of $\varepsilon_{\perp}$ in Fig. 4.11c; this reproduces experimental findings on the unchanged transparency of a smectic film under load, in similar conditions (Nishikawa et al. 1997).

However, the situation is the opposite when the load is applied parallel to the nematic director. We will focus on the effect the load has for two characteristic smectic LCE samples that differ in their preparation history. Namely, in the case of *sample I*, a freshly made network is crosslinked at 450 K, then equilibrated at this temperature for 27.2 ns, and finally heated up to 480 K for another 23.3 ns. In the case of *sample II*, the same fresh network was first heated to 500 K for 17.6 ns and then cooled down to 480 K for another 22.9 ns. The evolution of the backbone radius of gyration ratio $R_{\parallel}/R_{\perp}$, as well as the mesogen order parameters $S_{\parallel}$ and $S_{\perp}$ along and perpendicular to the load, respectively, are shown in Fig. 4.12c. The case of *sample I* under a load of $P_L = 73$atm is shown. All three properties, $R_{\parallel}/R_{\perp}$, $S_{\parallel}$, and $S_{\perp}$ undergo considerable changes. During the initial stage (1–10 ns), $R_{\parallel}/R_{\perp}$ changes gradually from an initial value of 0.4 to approximately 1, whereas $S_{\parallel}$ decreases from 0.75 to about 0.55 and $S_{\perp}$ increases from -0.34 to -0.1. At $t = 10$ns, the system undergoes a sharp transformation characterized by a jump of $R_{\parallel}/R_{\perp}$ up to 5, and a rapid exchange of values between $S_{\parallel}$ and $S_{\perp}$, which indicates director reorientation. The threshold value of $R_{\parallel}/R_{\perp}$, at which this transformation starts, is about 1.2–1.25. In the new state, with a reoriented nematic director, $R_{\parallel}/R_{\perp}$ increases further up to about 9–10, but with only minimal changes to $S_{\parallel}$ and $S_{\perp}$. The behavior of the sample in this latter state is very similar to the one observed in Fig. 4.12b, when the load is applied perpendicular to the nematic director. This comes as no surprise, since after the director reorientation takes place at time $t \approx 10$ ns in Fig. 4.12c, the new director is perpendicular to the load axis. The director reorientation is illustrated by snapshots presented in Fig. 4.13, frames d–f. The snapshots also confirm the integrity of the sample at all stages. One can also note that at an early stage of director reorientation ($t < 8.6$ns) the load somewhat reduces the defects found in the layered structure. After releasing the load, at time $t = 60$ns (see Fig. 4.12c), the mesogen order parameters do not change, whereas the backbone anisotropy decreases down to $R_{\parallel}/R_{\perp} \approx 2.5$. This value is exactly the reciprocal of the initial value $R_{\parallel}/R_{\perp} = 0.4$ at time $t = 0$, indicating that the reoriented smectic phase of *sample I* at the end of the simulation has the same properties as the initial one at $t = 0$ (taking into account the swap between the axes denoted as $\parallel$ and $\perp$).

Let us switch now to *sample II*, which differs from *sample I* by its thermal history, as already discussed above. A load of the same strength, $P_L = 73$atm, is applied at the same temperature, $T = 480$K, with the load axis parallel to the director. As a result of the load, *sample II* develops a stripe-like director pattern (with only two stripes within a single periodic box) during the first 1.5–2 ns, but in 4 ns time the sample fractures, as shown in Fig. 4.13, frames g–i. It is interesting to note, that both *sample I* and *sample II* have a similar defect in their lamellar structure before the load is applied (see Fig. 4.13 frames d and g, respectively). However, radically different director responses are found in these samples upon application of the load in the same direction and of the same amount. *Sample I* demonstrates a gradual reorientation of the director, whereas *sample II* develops a stripe-like pattern under load. As follows from the snapshots presented in Fig. 4.13, the layer normal for *sample I* at $t = 0$ is not exactly parallel to the Z axis. Therefore, the results obtained in our simulations can be related to the experiments performed on nematic LCEs when the direction of the applied load is not exactly perpendicular to the director. In this case, gradual director reorientation is found (Kundler and Finkelmann 1995; Roberts et al. 1997). *Sample II* at $t = 0$ demonstrates two smectic regions with slightly different angles between their respective layer normals and the Z axis. The formation of a stripe-like pattern can be explained in two possible ways. The first explanation is that the layer normal averaged over the sample volume is parallel to the Z axis. Then, this case is similar to the experiments on nematic LCEs when the load is applied perpendicular to the director, and stripe formation is also observed (Küpfer and Finkelmann 1991). The second explanation could be the presence of the defect which separates the two smectic regions in the initial configuration. Upon application of the load, the directors in each region rotate independently, which results in a V-shaped or chevron-like structure. Indeed, the wedge of this pattern is developed exactly at the defect position. As follows from these simulations, both the thermal history and, possibly, the existing defects in structure, play an important role in the kind of response developed under load. Similar remarks on the role of the preparation history of the sample on its behavior under stress were made earlier, in the experimental work of Zhang et al. (2006). These results lead us to believe that the simulations are correctly embodying the essential physics, but our model system is rather small to be able to study periodic stripe formation as found experimentally (Küpfer and Finkelmann 1991; Kundler and Finkelmann 1995, 1998; Nishikawa et al. 1997; Nishikawa and Finkelmann 1999; Verwey et al. 1996; Finkelmann et al. 1997; Biggins 2009), and discussed theoretically (Adams and Warner 2005; Fried and Sellers 2006).

4.4   Conclusions

In this chapter we consider equilibrium properties and stimuli response of liquid crystal polymers with side-chain molecular architecture. The semi-atomistic molecular dynamics simulation technique is employed, where groups of atoms are

represented as spherical and non-spherical bodies. Following the experimental data, we focus on several aspects of such systems that govern their properties and the response to external perturbations. These are: (a) the level of rigidity of the polymer backbone; (b) the amount of coupling between the polymer and liquid crystal subsystems; and (c) the existence of crosslinks.

Two characteristic models are considered, termed the weakly- and strongly-coupled models, where the naming reflects the amount of coupling between the polymer backbone and pendant mesogens. The former has a flexible backbone and long spacer of six to ten monomers, and is found to exhibit isotropic and smectic-A phases, in accordance with the experimental phase diagrams for real systems of this architecture. The smectic-A phase has a lamellar, sandwich-like internal structure, with backbones jammed in planes perpendicular to the nematic director. The diffusion of all its constituents, estimated in the course of our simulations, is severely hampered along the nematic director. On the contrary, the strongly-coupled model exhibits no ordered liquid crystal phases, and we concentrated mainly on an estimate for its glass transition temperature.

When the mesogens act as chromophores (the best known example being an azobenzene group), a number of related photo-mechanical effects are observed, e.g. surface relief grating formation. To model these effects we reduce the quantum photo-isomerization of azobenzene to the level of a classical field that reorients their *trans* isomers perpendicular to the light polarization. Then, we use the experimental evidence that free-floating droplets of the polymer P6a12 (flexible backbone, long spacer) contract along the polarization vector, whereas droplets of E1aP (backbone containing aromatic rings, short spacer) extend in this direction. Similar results are obtained in the experiments with an optical mask. The molecular details of P6a12 and E1aP map well onto the weakly- and strongly-coupled models, respectively. We found that for both models the photo-induced reorientation of chromophores is followed by repacking of the polymer backbones. However, in the case of the weakly-coupled model, the dominant effect is the photo-induced smectic–isotropic phase transition, which leads to the contraction of the volume element along the light polarization. For the case of the strongly-coupled model, the reorientation of stiff backbones is a dominant effect leading to the expansion of the volume element along the light polarization. The latter is irreversible only when the polymer is at or below the glass transition temperature, correlating well with the experimental results on recording of the surface gratings.

With crosslinking of the melt, a new set of memory effects emerge, related to the elasticity of the polymer network. To improve mapping of the properties of our relatively small model system onto those of a macro-sample, we use a controllable crosslinking algorithm applied in the smectic-A phase. The weakly crosslinked smectic elastomer is characterized by an increase of its smectic–isotropic transition temperature of about $5°$, as compared to its non-crosslinked counterpart; the shift is of the order of typical experimental values. The sample reproduces memory effects in its liquid-crystalline order and shape, when driven through the smectic–isotropic transition; the effect does not exist for a non-crosslinked system. When the elasto-mer is heated above the smectic–isotropic transition temperature and stretched, a

stress-induced smectic phase is observed. We also reproduce the experimentally observed anisotropy in the response of the smectic elastomer to a uniaxial load. In particular, smectic order is preserved when the system is stretched perpendicularly to the nematic director, even for a strain of about 200 %. On the contrary, when the load is applied parallel to the nematic director, one observes director reorientation or V-shaped stripes. To clarify the role of molecular architecture in the response of the smectic elastomer more precisely, significantly larger system sizes are required.

The results presented in this Chapter make some progress on the way of a more general agenda: simulation-based prediction of the macro-properties of polymer liquid crystals depending on the details of their molecular architecture. So far, the main achievement is in reproducing the existing experimental results and suggesting and verifying underlying microscopic mechanisms. More precise material–model bridging is required to be able to predict some new features or reproduce the existing effects on a more exact quantitative level. This program requires the use of precisely-tuned parametrized interaction potentials, as well as the use of large-scale system sizes.

References

Adams J, Warner M (2005) Elasticity of smectic-A elastomers. Phys Rev E 71(2):021708

Aharony A, Harris A (1996) Absence of self-averaging and universal fluctuations in random systems near critical points. Phys Rev Lett 77(18):3700–3703

Ahn S, Deshmukh P, Gopinadhan M, Osuji CO, Kasi RM (2011) Side-chain liquid crystalline polymer networks: exploiting nanoscale smectic polymorphism to design shape-memory polymers. ACS Nano 5(4):3085–3095

Allen MP, Tildesley DJ (1989) Computer simulation of liquids. Oxford University Press, Oxford

Assfalg N, Finkelmann H (1989) A composite of a nematic and an isotropic elastomer ± a rubber analogous to a "bimetal". Kaut Gummi Kunstst 52(10):677–678

Baldus O, Zilker S (2001) Surface relief gratings in photoaddressable polymers generated by cw holography. Appl Phys B Lasers Opt 72(4):425–427

Barillé R, Tajalli P, Kucharski S, Ortyl E, Nunzi JM (2010) Photoinduced deformation of azopolymer nanometric spheres. Appl Phys Lett 96(16):163104

Barrett CJ, Rochon PL, Natansohn AL (1998) Model of laser-driven mass transport in thin films of dye-functionalized polymers. J Chem Phys 109(4):1505

Barrett CJ, Mamiya J, Yager KG, Ikeda T (2007) Photo-mechanical effects in azobenzene-containing soft materials. Soft Matter 3(10):1249

Behl M, Lendlein A (2007) Shape-memory polymers. Mater Today 10(4):20–28

Berg RH, Hvilsted S, Ramanujam PS (1996) Peptide oligomers for holographic data storage. Nature 383(6600):505–508

Biggins JS (2009) Textured deformations in liquid crystal elastomers. Liq Cryst 36 (10–11):1139–1156

Binder K (1986) Spin glasses: experimental facts, theoretical concepts, and open questions. Rev Mod Phys 58(4):801–976

Bladon P, Terentjev E, Warner M (1993) Transitions and instabilities in liquid crystal elastomers. Phys Rev E 47(6):R3838–R3840

Bladon P, Warner M, Terentjev EM (1994) Orientational order in strained nematic networks. Macromolecules 27(24):7067–7075

Bublitz D, Helgert M, Fleck B, Wenke L, Hvilsted S, Ramanujam P (2000) Photoinduced deformation of azobenzene polyester films. Appl Phys B Lasers Opt 70(6):863–865

Bublitz D, Fleck B, Wenke L (2001) A model for surface-relief formation in azobenzene polymers. Appl Phys B Lasers Opt 72(8):931–936

Camacho-Lopez M, Finkelmann H, Palffy-Muhoray P, Shelley M (2004) Fast liquid-crystal elastomer swims into the dark. Nat Mater 3(5):307–310

Chung TS (ed) (2008) Thermotropic liquid crystalline polymers. Technomic, Lancaster

Cladis PE (2001) Phase transitions in liquid crystalline elastomers. A fundamental aspect of lces as artificial muscles. In: Ehrhard P, Riley D (eds) Proceedings of Euromech colloquium 408. Kluewer Academic, Dordecht, pp 429–483

Cleaver D, Care C, Allen M, Neal M (1996) Extension and generalization of the Gay-Berne potential. Phys Rev E 54(1):559–567

Collings PJ, Hird M (2001) Introduction to liquid crystals. Taylor and Francis, London

Davis FJ, Mitchell GR (1996) Liquid crystal elastomers: controlled crosslinking in the liquid crystal phase. Polymer 37(8):1345–1351

Degert C, Davidson P, Megtert S, Petermann D, Mauzac M (1992) X-ray diffraction by liquid-crystalline elastomers. Liq Cryst 12(5):779–798

Dimitrova A (2000) Investigation of the main chain orientation in side-chain liquid crystalline polymers by natural abundance ^{13}C NMR. Ph.D. thesis, University of Halle

Doi M, Edwards SF (1994) The theory of polymer dynamics. Clarendon Press, Oxford

Finkelmann H, Kock HJ, Rehage G (1981) Investigations on liquid crystalline polysiloxanes 3. Liquid crystalline elastomers – a new type of liquid crystalline material. Makromol Chem Rapid Commun 2(4):317–322

Finkelmann H, Kock HJ, Gleim W, Rehage G (1984) Investigations on liquid crystalline polysiloxanes, 5. Orientation of LC-elastomers by mechanical forces. Makromol Chem Rapid Commun 5(5):287–293

Finkelmann H, Kundler I, Terentjev EM, Warner M (1997) Critical stripe-domain instability of nematic elastomers. J Phys II 7(8):1059–1069

Freiberg S, Lagugné-Labarthet F, Rochon P, Natansohn A (2003) Synthesis and characterization of a series of azobenzene-containing side-chain liquid crystalline polymers. Macromolecules 36(8):2680–2688

Fried E, Sellers S (2006) Soft elasticity is not necessary for striping in nematic elastomers. J Appl Phys 100(4):043521

Gaididei Y, Christiansen P, Ramanujam P (2002) Theory of photoinduced deformation of molecular films. Appl Phys B Lasers Opt 74(2):139–146

Gallani J, Hilliou L, Martinoty P, Keller P (1994) Abnormal viscoelastic behavior of side-chain liquid-crystal polymers. Phys Rev Lett 72(13):2109–2112

Gay JG, Berne BJ (1981) Modification of the overlap potential to mimic a linear site-site potential. J Chem Phys 74(6):3316

Han J, Gee RH, Boyd RH (1994) Glass transition temperatures of polymers from molecular dynamics simulations. Macromolecules 27(26):7781–7784

Hill R (1984) On macroscopic effects of heterogeneity in elastoplastic media at finite strain. Math Proc Camb 95(03):481

Hill R (1985) On the micro-to-macro transition in constitutive analyses of elastoplastic response at finite strain. Math Proc Camb 98(03):579

Hirschmann H, Roberts P, Davis F, Guo W, Hasson C, Mitchell G (2001) Liquid crystalline elastomers: the relationship between macroscopic behaviour and the level of backbone anisotropy. Polymer 42(16):7063–7071

Holme NCR, Nikolova L, Hvilsted S, Rasmussen PH, Berg RH, Ramanujam PS (1999) Optically induced surface relief phenomena in azobenzene polymers. Appl Phys Lett 74(4):519

Hvilsted S, Ramanujam PS (2001) The azobenzene optical storage puzzle – demands on the polymer scaffold? Monatsh Chem 132(1):43–51

Ichimura K (2000) Photoalignment of liquid-crystal systems. Chem Rev 100(5):1847–1874

Ikeda T (2003) Photomodulation of liquid crystal orientations for photonic applications. J Mater Chem 13(9):2037–2057

Ikeda T, Horiuchi S, Karanjit DB, Kurihara S, Tazuke S (1990) Photochemically induced isothermal phase transition in polymer liquid crystals with mesogenic phenyl benzoate side chains, 2. Photochemically induced isothermal phase transition behaviors. Macromolecules 23 (1):42–48

Ikeda T, Yoneyama S, Yamamoto T, Hasegawa M (2002) Refractive-index modulation by means of photosensitive liquid crystals. Mol Cryst Liq Cryst 375:45–60

Ikeda T, Mamiya J, Yu Y (2007) Photomechanics of liquid-crystalline elastomers and other polymers. Angew Chem Int Ed 46(4):506–528

Ilnytskyi J, Wilson MR (2001) A domain decomposition molecular dynamics program for the simulation of flexible molecules with an arbitrary topology of Lennard-Jones and/or Gay-Berne sites. Comput Phys Commun 134(1):23–32

Ilnytskyi J, Saphiannikova M, Neher D (2006) Photo-induced deformations in azobenzene-containing side-chain polymers: molecular dynamics study. Condens Matter Phys 9(1):87–94

Ilnytskyi JM, Neher D (2007) Structure and internal dynamics of a side chain liquid crystalline polymer in various phases by molecular dynamics simulations: a step towards coarse graining. J Chem Phys 126(17):174905

Ilnytskyi JM, Wilson MR (2002) A domain decomposition molecular dynamics program for the simulation of flexible molecules of spherically-symmetrical and nonspherical sites, II. Extension to NVT and NPT ensembles. Comput Phys Commun 148(1):43–58

Ilnytskyi JM, Neher D, Saphiannikova M (2011) Opposite photo-induced deformations in azobenzene-containing polymers with different molecular architecture: molecular dynamics study. J Chem Phys 135(4):044901

Ilnytskyi JM, Saphiannikova M, Neher D, Allen MP (2012) Modelling elasticity and memory effects in liquid crystalline elastomers by molecular dynamics simulations. Soft Matter 8 (43):11123–11134

Kandjani SA, Barille R, Dabos-Seignon S, Nunzi JM, Ortyl E, Kucharski S (2005) Incoherent light-induced self-organization of molecules. Opt Lett 30(23):3177

Keller P, Carvalho B, Cotton JP, Lambert M, Moussa F, Pépy G (1985) Side chain mesomorphic polymers: studies of labelled backbones by neutron scattering. J Phys Lett (Paris) 46 (22):1065–1071

Kim DY, Tripathy SK, Li L, Kumar J (1995) Laser-induced holographic surface relief gratings on nonlinear optical polymer films. Appl Phys Lett 66(10):1166

Kirste RG, Ohm HG (1985) The conformation of liquid-crystalline polymers as revealed by neutron scattering. Makromol Chem Rapid Commun 6(3):179–185

Kumar J, Li L, Jiang XL, Kim D, Lee TS, Tripathy S (1998) Gradient force: The mechanism for surface relief grating formation in azobenzene functionalized polymers. Appl Phys Lett 72 (17):2096

Kundler I, Finkelmann H (1995) Strain-induced director reorientation in nematic liquid single crystal elastomers. Macromol Rapid Commun 16(9):679–686

Kundler I, Finkelmann H (1998) Director reorientation via stripe-domains in nematic elastomers: influence of cross-link density, anisotropy of the network and smectic clusters. Macromol Chem Phys 199(4):677–686

Küpfer J, Finkelmann H (1991) Nematic liquid single crystal elastomers. Makromol Chem Rapid Commun 12(12):717–726

Lefin P, Fiorini C, Nunzi JM (1998) Anisotropy of the photo-induced translation diffusion of azobenzene dyes in polymer matrices. Pure Appl Opt 7(1):71–82

Legge CH, Davis FJ, Mitchell GR (1991) Memory effects in liquid crystal elastomers. J Phys II 1 (10):1253–1261

Lyulin AV, Balabaev NK, Michels MAJ (2003) Molecular-weight and cooling-rate dependence of simulated T_g for amorphous polystyrene. Macromolecules 36(22):8574–8575

Matouš K, Geubelle PH (2005) Multiscale modelling of particle debonding in reinforced elastomers subjected to finite deformations. Int J Numer Meth Eng 65(2):190–223

McBride C, Wilson MR (1999) Molecular dynamics simulations of a flexible liquid crystal. Mol Phys 97(4):511–522

Mechau N, Neher D, Börger V, Menzel H, Urayama K (2002) Optically driven diffusion and mechanical softening in azobenzene polymer layers. Appl Phys Lett 81(25):4715

Mechau N, Saphiannikova M, Neher D (2005) Dielectric and mechanical properties of azobenzene polymer layers under visible and ultraviolet irradiation. Macromolecules 38(9):3894–3902

Michel JC, Moulinec H, Suquet P (1999) Effective properties of composite materials with periodic microstructure: a computational approach. Comput Method Appl Mech Eng 172 (1–4):109–143

Michl J, Thulstrup EW (1995) Spectroscopy with polarized light: solute alignment by photoselection, liquid crystal, polymers, and membranes. Corrected Software Edition. VCH Publishers, New York

Mitchell G, Davis F, Guo W, Cywinski R (1991) Coupling between mesogenic units and polymer backbone in side-chain liquid crystal polymers and elastomers. Polymer 32(8):1347–1353

Mitchell G, Davis F, Guo W (1993) Strain-induced transitions in liquid-crystal elastomers. Phys Rev Lett 71(18):2947–2950

Mitchell GR, Davis FJ, Ashman A (1987) Structural studies of side-chain liquid crystal polymers and elastomers. Polymer 28(4):639–647

Mitchell GR, Coulter M, Davis FJ, Guo W (1992) The effect of the spacer length on the nature of coupling in side chain liquid crystals polymers and elastomers. J Phys II 2(5):1121–1132

Natansohn A, Rochon P (1999) Photoinduced motions in azobenzene-based amorphous polymers: possible photonic devices. Adv Mater 11(16):1387–1391

Nishikawa E, Finkelmann H (1999) Smectic-A liquid single crystal elastomers - strain induced break-down of smectic layers. Macromol Chem Phys 200(2):312–322

Nishikawa E, Finkelmann H, Brand HR (1997) Smectic A liquid single crystal elastomers showing macroscopic in-plane fluidity. Macromol Rapid Commun 18(2):65–71

Oliveira ON, Kumar LL, Tripathy SK (2002) Surface-relief gratings on azobenzene-containing films. In: Sekkat Z, Knoll W (eds) Photoreactive organic thin films. Academic, California, pp 429–483

Parrinello M, Rahman A (1981) Polymorphic transitions in single crystals: A new molecular dynamics method. J Appl Phys 52(12):7182

Pedersen T, Johansen P, Holme N, Ramanujam P, Hvilsted S (1998) Mean-field theory of photoinduced formation of surface reliefs in side-chain azobenzene polymers. Phys Rev Lett 80(1):89–92

Rasmussen PH, Ramanujam PS, Hvilsted S, Berg RH (1999) A remarkably efficient azobenzene peptide for holographic information storage. J Am Chem Soc 121(20):4738–4743

Roberts PMS, Mitchell GR, Davis FJ, Pople JA (1997) Mechanical switching and soft elasticity in liquid crystal elastomers. Mol Cryst Liq Cryst 299(1):181–186

Rochon P, Batalla E, Natansohn A (1995) Optically induced surface gratings on azoaromatic polymer films. Appl Phys Lett 66(2):136

Rutloh M, Stumpe J, Stachanov L, Kostromin S, Shibaev V (2000) Influence of liquid crystallinity and aggregation on photo-orientation. Mol Cryst Liq Cryst 352(1):149–157

Ryckaert JP, Bellemans A (1975) Molecular dynamics of liquid n-butane near its boiling point. Chem Phys Lett 30(1):123–125

Sainova D, Zen A, Nothofer HG, Asawapirom U, Scherf U, Hagen R, Bieringer T, Kostromine S, Neher D (2002) Photoaddressable alignment layers for fluorescent polymers in polarized electroluminescence devices. Adv Funct Mater 12(1):49

Saphiannikova M, Neher D (2005) Thermodynamic theory of light-induced material transport in amorphous azobenzene polymer films. J Phys Chem B 109(41):19428–19436

Saphiannikova M, Geue TM, Henneberg O, Morawetz K, Pietsch U (2004) Linear viscoelastic analysis of formation and relaxation of azobenzene polymer gratings. J Chem Phys 120 (8):4039

Schätzle J, Kaufhold W, Finkelmann H (1989) Nematic elastomers: the influence of external mechanical stress on the liquid-crystalline phase behavior. Makromolekul Chem 190 (12):3269–3284

Shenoy DK, Thomse III DL, Srinivasan A, Keller P, Ratna BR (2002) Carbon coated liquid crystal elastomer film for artificial muscle applications. Sensors Actuators A Phys 96(2–3):184–188

Spillmann CM, Naciri J, Martin BD, Farahat W, Herr H, Ratna BR (2007) Stacking nematic elastomers for artificial muscle applications. Sensors Actuators A Phys 133(2):500–505

Stiller B, Geue T, Morawetz K, Saphiannikova M (2005) Optical patterning in azobenzene polymer films. J Microsc 219(3):109–114

Stimson LM, Wilson MR (2005) Molecular dynamics simulations of side chain liquid crystal polymer molecules in isotropic and liquid-crystalline melts. J Chem Phys 123(3):034908

Stracke A, Wendorff JH, Goldmann D, Janietz D, Stiller B (2000) Gain effects in optical storage: thermal induction of a surface relief grating in a smectic liquid crystal. Adv Mater 12 (4):282–285

Symons AJ, Davis FJ, Mitchell GR (1993) Liquid crystal elastomers interaction between the network and smectic ordering. Liq Cryst 14(3):853–860

Symons AJ, Davis FJ, Mitchell GR (1999) Side-chain liquid crystalline elastomers: the relationship between the orientational ordering of the polymer backbone and the length of the coupling chain. Polymer 40(19):5365–5370

Tajbakhsh A, Terentjev E (2001) Spontaneous thermal expansion of nematic elastomers. Eur Phys J E 6(2):181–188

Toshchevikov V, Saphiannikova M (2014) Theory of light-induced deformation of azobenzene elastomers: effects of the liquid-crystalline interactions and biaxiality. J Phys Chem B 118 (42):12297–12309. doi10.1021/jp5063226. http://dx.doi.org/10.1021/jp5063226

Toshchevikov V, Saphiannikova M, Heinrich G (2009) Microscopic theory of light-induced deformation in amorphous side-chain azobenzene polymers. J Phys Chem B 113 (15):5032–5045

Toshchevikov VP, Grenzer MS, Heinrich G (2012) Effects of the liquid-crystalline order on the light-induced deformation of azobenzene elastomers. In: Zamboni R, Kajzar F, Szep AA (eds) Optical materials and biomaterials in security and defence systems technology IX, SPIE

Veer PU, Pietsch U, Rochon PL, Saphiannikova M (2008) Temperature dependent analysis of grating formation on azobenzene polymer films. Mol Cryst Liq Cryst 486(1):66/[1108]–78/ [1120]

Veer PU, Pietsch U, Saphiannikova M (2009) Time and temperature dependence of surface relief grating formation in polymers containing azobenzene groups with different dipole moment. J Appl Phys 106(1):014909

Verwey GC, Warner M, Terentjev EM (1996) Elastic instability and stripe domains in liquid crystalline elastomers. J Phys II 6(9):1273–1290

Viswanathan NK, Kim DY, Bian S, Williams J, Liu W, Li L, Samuelson L, Kumar J, Tripathy SK (1999) Surface relief structures on azo polymer films. J Mater Chem 9(9):1941–1955

Vlugt TJH, Krishna R, Smit B (1999) Molecular simulations of adsorption isotherms for linear and branched alkanes and their mixtures in silicalite. J Phys Chem B 103(7):1102–1118

Warner M, Terentjev E (1996) Nematic elastomers – a new state of matter? Prog Polym Sci 21 (5):853–891

Warner M, Terentjev E (2003) Thermal and photo-actuation in nematic elastomers. Macromol Symp 200(1):81–92

Warner M, Gelling KP, Vilgis TA (1988) Theory of nematic networks. J Chem Phys 88 (6):4008–4013

Weilepp J, Brand HR (1996) Director reorientation in nematic-liquid-single-crystal elastomers by external mechanical stress. Europhys Lett 34(7):495–500

Wilson MR (1997) Molecular dynamics simulations of flexible liquid crystal molecules using a Gay-Berne/Lennard-Jones model. J Chem Phys 107(20):8654

Wilson MR, Ilnytskyi JM, Stimson LM (2003) Computer simulations of a liquid crystalline dendrimer in liquid crystalline solvents. J Chem Phys 119(6):3509

Wilson MR, Stimson LM, Ilnytskyi JM, Hughes ZE (2005) Computer simulations of liquid crystal polymers and dendrimers. In: Pasini P, Zannoni C, Žumer S (eds) NATO science series II: mathematics, physics and chemistry. Springer, New York, pp 57–81

Wiseman S, Domany E (1998) Self-averaging, distribution of pseudocritical temperatures, and finite size scaling in critical disordered systems. Phys Rev E 58(3):2938–2951

Zen A, Neher D, Bauer C, Asawapirom U, Scherf U, Hagen R, Kostromine S, Mahrt RF (2002) Polarization-sensitive photoconductivity in aligned polyfluorene layers. Appl Phys Lett 80 (25):4699

Zhang F, Heiney P, Srinivasan A, Naciri J, Ratna B (2006) Structure of nematic liquid crystalline elastomers under uniaxial deformation. Phys Rev E 73(2)

Zilker SJ, Bieringer T, Haarer D, Stein RS, van Egmond JW, Kostromine SG (1998) Holographic data storage in amorphous polymers. Adv Mater 10(11):855–859